The WAM Model—A Third Generation Ocean Wave Prediction Model

THE WAMDI GROUP*

ABSTRACT

A third generation wave model is presented that integrates the basic transport equation describing the evolution of a two-dimensional ocean wave spectrum without additional ad hoc assumptions regarding the spectral shape. The three source functions describing the wind input, nonlinear transfer, and white-capping dissipation are prescribed explicitly. An additional bottom dissipation source function and refraction terms are included in the finite-depth version of the model. The model was calibrated against fetch-limited wave growth data. Only two tuning parameters are introduced in the white-capping dissipation source function. The model runs on a spherical latitude–longitude grid for an arbitrary region of the ocean. Hindcast results are shown for six North Atlantic–North Sea storms, three Gulf of Mexico hurricanes, and a global run for the SEASAT period. The agreement with measurements is encouraging.

1. Introduction

Since the pioneering paper of Gelci et al. (1957), numerical wave prediction models have been formulated in terms of the basic transport equation for the two-dimensional wave spectrum. The general structure of the source function of the (deep water) transport equation, consisting of a superposition of the energy input by the wind, S_{in}, normally represented as the sum of a Phillips (1957) and Miles (1957) term, the nonlinear transfer S_{nl} due to resonant wave–wave interactions, and the dissipation S_{ds} due to white capping and turbulence, has also been known for more than 25 years (Hasselmann 1960). Nevertheless, none of the wave models developed since this time have actually computed the wave spectrum from first principles alone from the spectral transport equation. Some form of additional ad hoc assumptions have always been introduced to force the spectrum to comply with some preconceived notions of wave development that could

not be readily expressed by (and in some cases were not consistent with) the source function used in the transport equation (cf. SWAMP Group 1985).

First generation wave models developed in the 1960s and early 1970s avoided the problem of explicitly modeling the complete energy balance. In particular, the details of how the spectrum attained its equilibrium form were not specified. In these models, it was assumed that the wave components suddenly stopped growing when they reached a universal saturation level (Phillips 1958). The saturation spectrum, represented by Phillips' one-dimensional f^{-5} frequency spectrum and an empirical equilibrium directional distribution, was prescribed. Thus, for growing windseas, the prognostic region of the modeled spectrum was, in effect, limited to wave components in the neighborhood of the spectral peak.

It is generally recognized today that a universal high-frequency equilibrium spectrum of the form originally proposed by Phillips does not exist. The high-frequency region of the spectrum depends not only on the white capping process, but also on the local wind input and on the low-frequency regions of the spectrum to which it is coupled via the nonlinear transfer. It has now also become clear that first generation wave models exhibit basic quantitative shortcomings: they overestimated the wind input and underestimated the strength of the nonlinear transfer by almost an order of magnitude.

In the 1970s, extensive wave growth experiments (Mitsuyasu 1968, 1969; Hasselmann et al. 1973) and direct measurements of the wind input to the waves (Snyder et al. 1981; Hasselmann et al. 1986) fundamentally changed the view of the spectral energy balance on which the first generation models had been based, leading to the development of second generation

* The Wave Model Development and Implementation Group: S. Hasselmann, K. Hasselmann and E. Bauer, *Max-Planck-Institut für Meteorology, Hamburg.* P. A. E. M. Janssen and G. J. Komen, *Koninklijk Nederlands Meteorologisch Instituut, De Bilt.* L. Bertotti and P. Lionello, *Laboratorio per lo Studio della Dinamica delle Grandi Masse, Venezia.* A. Guillaume, *Météorologie Nationale, Paris.* V. C. Cardone and J. A. Greenwood, *Oceanweather Inc., Cos Cob.* M. Reistad, *The Norwegian Meteorological Institute, Bergen.* L. Zambresky, *European Centre for Medium Range Weather Forecasts, Reading,* and *GKSS Forschungszentrum Geesthacht GmbH, Geesthacht.* J. A. Ewing, *Institute of Oceanographic Sciences, Wormley.*

Corresponding author address: Dr. Klaus Hasselmann, Max-Planck Institut für Meteorologie, Bundesstrasse 55, D-2000 Hamburg 13, West Germany.

wave models. However, for these models also, restrictions resulting from the simplified nonlinear transfer parameterization effectively required the spectral shape of the windsea spectrum to be prescribed for frequencies higher than the peak frequency. The specification of the spectral shape was introduced either at the outset in the formulation of the transport equation itself (parametrical or hybrid models) or as a side condition in the computation of the spectrum (discrete models). Although the adjustment to a quasi-universal spectral shape could be justified theoretically by two scaling arguments for typical synoptic-scale wind fields (Hasselmann et al. 1976), the second generation models were unable to properly simulate complex windseas generated by rapidly changing wind fields, for example, in hurricanes, intense, small-scale cyclones or fronts. The models also encountered basic difficulties in treating the transition between windsea and swell.

The shortcomings of first and second generation models have been identified and discussed in detail in the SWAMP (1985) wave-model intercomparison study. Although both first and second generation wave models can be tuned to provide useful results for certain classes of wind fields—and most models considered in the study had indeed proven their value in an operational framework—the study demonstrated that none of the existing wave models were applicable for all wind fields, and that none were reliable for extreme situations for which wave forecasts are often most needed.

In the case of second generation wave models, the problems are largely numerical rather than physical. Techniques for overcoming these difficulties were suggested already in SWAMP (1985). It was proposed that third generation models should be developed, based on these techniques, in which the wave spectrum was computed alone by integration of the basic spectral transport equation, without any prior restriction of the spectral shape. The model presented in this paper represents the first implementation of such a third generation wave model. The work was carried out within the framework of the WAM (Wave Modeling) program, which was initiated after the completion of the SWAMP Study (cf. Komen 1985).

To remove the restrictions on the spectral shape, two steps were necessary.

First, a parameterization of the exact nonlinear transfer source function had to be developed that contained the same number of degrees of freedom as the spectrum itself. (Computations of the exact five-dimensional integral representing the continuum of all resonant interactions for the entire spectrum are still too time consuming, even with present day vector computers, to be incorporated in operational wave models.) As discussed in the SWAMP Study, wave models in which the numbers of degrees of freedom of the spectrum and the nonlinear transfer parameterization are not matched are generally unstable. In fact,

the restrictions in the spectral shape of second generation models result essentially from the need to adjust the number of degrees of freedom of the spectrum to the rather simple nonlinear parameterizations used in these models. The present model uses the discrete interaction approximation of Hasselmann et al. (1985), which retains the same cubic operator structure as the original Boltzmann integral (see also Hasselmann and Hasselmann 1981 and Young et al. 1987).

Second, the energy balance had to be closed by specifying the unknown dissipation source function. (The input source function was adopted from the measurements of Snyder et al. 1981). The dissipation source function used in the present model corresponds to the form proposed by Komen et al. (1984) on the basis of a series of numerical integrations of the transport equation using prescribed source functions for the input (from Snyder et al. 1981) and with exact computations of the nonlinear transfer. The dissipation was tuned to reproduce the observed fetch-limited wave growth and the fully developed Pierson–Moskowitz spectrum.

Once the source functions have been determined by tests for the fetch-limited, uniform wind case, the model is completely specified and should be applicable to arbitrary wind fields without further tuning. We present verifications of a regional version of the model for nine hindcast studies consisting of six North Atlantic–North Sea storms and three Gulf of Mexico hurricanes. As application of the global version of the model, we show also examples of global wave hindcasts computed from the gridded global surface stress fields constructed by Atlas et al. (1987) from SEASAT scatterometer data and conventional meteorological data using a data assimilation method.

The source functions in the present model will undoubtedly need to be modified and improved as further experience is gained in the operation of the model. However, it is hoped that by presenting a third generation wave model, future model improvements can be introduced at the appropriate level, namely in the source functions representing the physics, rather than by modifying the form of the resultant wave spectrum.

The model is formulated in spherical latitude–longitude coordinates and can be run for an arbitrarily specified global or regional grid. It may be operated in a deep or shallow water mode and with a first or second order propagation scheme. An implicit integration method is used in order to maintain an acceptable time step Δt of the order of 10 to 20 minutes for all spectral components, including the highest prognostic frequency components of the model, whose response time is considerably smaller than Δt. The model is fully vectorized and can be run, with minor editing switches, on either CRAY or CYBER-205 computers. More details on the WAM model system, including pre- and post-processing packages, are given in Hasselmann (1987).

The deep-water formulation of the model is described in section 2, while section 3 lists the extensions needed for shallow water. Numerical aspects of the implicit integration method and the advection schemes are discussed in section 4. In section 5 the fetch limited growth results are shown for deep and shallow water. Verifications of the model for a series of six North Atlantic hindcast studies (the "WHIST" storm cases) and three Gulf of Mexico hurricane cases are presented in sections 6 and 7, respectively. The results of the global integrations for the SEASAT period are presented in section 8. Section 9 gives a summary of the conclusions and an outlook on future developments.

2. Formulation of the model—deep water case

The evolution of the two-dimensional ocean wave spectrum $F(f, \theta, \phi, \lambda, t)$ with respect to frequency f and direction θ (measured clockwise relative to true north) as a function of latitude ϕ and longitude λ on the spherical earth is governed by the transport equation

$$\frac{\partial F}{\partial t} + (\cos\phi)^{-1} \frac{\partial}{\partial \phi} (\dot{\phi} \cos\phi F)$$

$$+ \frac{\partial}{\partial \lambda} (\dot{\lambda} F) + \frac{\partial}{\partial \theta} (\dot{\theta} F) = S \quad (2.1)$$

where S is the net source function describing the change of energy of a propagating wave group and

$$\dot{\phi} = \frac{d\phi}{dt} = v R^{-1} \cos\theta \quad (2.2)$$

$$\dot{\lambda} = \frac{d\lambda}{dt} = v \sin\theta (R \cos\phi)^{-1} \quad (2.3)$$

$$\dot{\theta} = \frac{d\theta}{dt} = v \sin\theta \tan\phi R^{-1} \quad (2.4)$$

represent the rates of change of the position and propagation direction of a wave packet traveling along a great circle path (cf. appendix A). Here $v = g/4\pi f$ denotes the group velocity, g the acceleration of gravity, and R the radius of the earth. The equations apply for waves in water of infinite depth.

The generalization of the standard Cartesian geometry transport equation to the spherical geometry form (2.1) follows (cf. Groves and Melcer 1961) from the energy conservation equation

$$\frac{\partial \hat{F}}{\partial t} + \frac{\partial}{\partial \phi} (\dot{\phi}\hat{F}) + \frac{\partial}{\partial \lambda} (\dot{\lambda}\hat{F}) + \frac{\partial}{\partial \theta} (\dot{\theta}\hat{F}) = S \quad (2.5)$$

for the spectral density $\hat{F}(f, \theta, \phi, \lambda)$ with respect to the four-dimensional phase space $(f, \theta, \phi, \lambda)$. Here $\hat{F}$ is related to the normal spectral density F with respect to a local Cartesian frame (x, y) through $\hat{F}(dfd\theta d\phi d\lambda) = F(dfd\theta dxdy)$, or

$$\hat{F} = FR^2 \cos\phi. \quad (2.6)$$

Substitution of (2.6) into (2.5) yields (2.1).

The structure of the transport equations (2.1)–(2.4) carries over to the finite depth case [note that the great circle propagation equations already include a refraction term, Eq. (2.4)]. However, modifications need to be introduced in the expression for the group velocity, in the refraction equation (2.4), and in the form of the source function (cf. section 3).

The source function for the deep water case may be represented as a superposition of the wind input, non-linear transfer, and white capping dissipation source functions,

$$S = S_{in} + S_{nl} + S_{ds}. \quad (2.7)$$

The wind input source function was adopted from Snyder et al. (1981). However, following Komen et al. (1984), their relation was scaled in terms of the friction velocity u_* rather than the wind speed U_5 at 5 m height:

$$S_{in} = \beta F \quad (2.8)$$

where

$$\beta = \max\left\{0, 0.25 \frac{\rho_a}{\rho_w} \left(28 \frac{u_*}{c} \cos\theta - 1\right)\right\} \omega \quad (2.9)$$

and $\omega = 2\pi f$, ρ_a (ρ_w) is density of air (water).

Scaling of the wind input in terms of u_* is consistent with Charnock's (1955) original boundary layer arguments and appears more appealing theoretically than scaling with respect to the wind speed at a given height (cf. discussions in Komen et al. 1984; Janssen and Komen 1985). Empirically, it tends to yield a closer agreement of wave growth data obtained by different groups under different wind conditions (Janssen et al. 1987) and is supported by the hindcast cases presented in sections 7 and 8. (Recent studies by Donelan 1987; Donelan and Pierson 1987, however, suggest that improved agreement with data can be obtained by replacing the wind speed U_5 in the formula of Snyder et al. by the wind speed at a half-wavelength height above the surface. This can also be interpreted as u_* scaling, but with a different form of the input function. This question should be resolved by further numerical experiments.)

The dissipation source function is based on the form

$$S_{ds} = -3.33 \cdot 10^{-5} \bar{\omega} (\omega/\bar{\omega})^2 (\bar{\alpha}/\bar{\alpha}_{PM})^2 F \quad (2.10)$$

proposed by Komen et al. (1984), where

$$\bar{\omega} = E^{-1} \int\int F(f, \theta)\omega df d\theta \quad (2.11)$$

denotes the mean frequency,

$$E = \int\int F(f, \theta) df d\theta \quad (2.12)$$

is the total energy (surface elevation variance), α is an integral wave steepness parameter defined by

$$\bar{\alpha} = E\bar{\omega}^4 g^{-2}, \qquad (2.13)$$

and

$$\bar{\alpha}_{PM} = 4.57 \cdot 10^{-3} \qquad . \quad (2.14)$$

is the theoretical value of $\bar{\alpha}$ for a Pierson–Moskowitz spectrum. The quasi-linear dependence of S_{ds} on F and the dependence of the proportionality factor on the square of the frequency is consistent with the white capping dissipation function derived by Hasselmann (1974).

For implementation in the present model, the expression (2.10) was slightly modified by replacing the mean frequency $\bar{\omega}$ by the inverse of the mean period,

$$\hat{\omega} = \left[E^{-1} \int F(f, \theta)\omega^{-1} df d\theta \right]^{-1}. \qquad (2.15)$$

It was found that this enhanced the stability of the implicit integration scheme (enabling a larger time step). Introducing the new definitions and slightly reducing the constant, the model dissipation source was then taken as

$$S_{ds} = -2.33 \cdot 10^{-5} \hat{\omega}(\omega/\hat{\omega})^2 (\hat{\alpha}/\hat{\alpha}_{PM})^2 F \qquad (2.16)$$

where

$$\hat{\alpha} = E\hat{\omega}^4 g^{-2} \qquad (2.17)$$

$$\hat{\alpha}_{PM} = 0.66\bar{\alpha}_{PM}. \qquad (2.18)$$

The nonlinear source function S_{nl} was represented by the discrete interaction operator parameterization proposed by Hasselmann et al. (1985). This retains the basic form of the exact nonlinear transfer expression,

$$S_{nl}^{exact}(k_4) = \int \omega_4 \sigma \delta(k_1 + k_2 - k_3 - k_4)$$

$$\times \delta(\omega_1 + \omega_2 - \omega_3 - \omega_4)[n_1 n_2(n_3 + n_4)$$

$$- n_3 n_4(n_1 + n_2)]dk_1 dk_2 dk_3 \qquad (2.19)$$

where $n_j = F(k_j)/\omega_j$ denotes the action spectrum and the coefficient $\sigma(k_1, k_2, k_3, k_4)$ describes the coupling strength of a resonantly interacting wavenumber quadruplet k_1, k_2, k_3, k_4. However, the five-dimensional continuum of all resonant quadruplets (three integration dimensions and two dimensions for k_4) is reduced to a two-dimensional continuum by considering only a (mirror symmetrical) pair of discrete interaction configurations. (Two continuous dimensions are still needed to define the magnitude and direction of the reference wavenumber vector scaling the interaction configuration.)

Formally, the discrete interaction approximation may be written in the form

$$S_{nl}^{di}(k_4) = \sum_{\gamma=1,2} A_\gamma \omega_4 [n_1{}^\gamma n_2{}^\gamma (n_3{}^\gamma + n_4{}^\gamma)$$

$$- n_3{}^\gamma n_4{}^\gamma (n_1{}^\gamma + n_2{}^\gamma)] \qquad (2.20)$$

where A_γ are coupling coefficients and the action densities

$$n_i{}^\gamma = F(k_i{}^\gamma)/\omega_i{}^\gamma, \quad i = 1, 2, 3; \quad \gamma = 1, 2 \qquad (2.21)$$

are evaluated at discrete wavenumbers $k_i{}^\gamma = T_i{}^\gamma k_4$, which are related to the reference wavenumber k_4 through fixed linear transformations $T_i{}^\gamma$. In practice, S_{nl}^{di} is not computed using (2.20) but by the symmetrical integration method described in Hasselmann and Hasselmann (1985), in which the energy changes occurring in all four wavenumbers of a given interaction configuration are evaluated simultaneously (this is the reason we included k_4 as well as the interaction integral (2.19) in counting dimensions above).

The discrete interaction parameterization has been tested for fetch and duration limited wave growth and turning wind cases, with satisfactory results (Hasselmann et al. 1985; Young et al. 1987).

The model contains 25 frequency bands on a logarithmic scale, with $\Delta f/f = 0.1$, spanning a frequency range $f_{max}/f_{min} = 9.8$ and 12 directional bands (30° resolution). The frequency units can be selected arbitrarily. In all hindcast studies presented below, the frequency interval extended from 0.042 to 0.41 Hz. A 15° resolution model has also been tested but was not applied in the present study.

Beyond the high-frequency limit f_{hf} of the prognostic region of the spectrum, an f^{-4} tail is added, with the same directional distribution as the last band of the prognostic region,

$$F(f, \theta) = F(f_{hf}, \theta)\left(\frac{f}{f_{hf}}\right)^{-4} \quad \text{for} \quad f > f_{hf}. \qquad (2.22)$$

The high-frequency limit is set as

$$f_{hf} = \min\{f_{max}, \max(2.5\bar{f}, 4f_{PM})\}. \qquad (2.23)$$

Thus, the high-frequency extent of the prognostic region is scaled for young waves by the mean frequency and for more developed windseas by the "wind frequency" f_{PM}. A dynamic high-frequency cutoff, f_{hf}, rather than a fixed cutoff at f_{max} is necessary to avoid excessive disparities in the response time scales within the spectrum.

A diagnostic tail needs to be added for $f > f_{hf}$ to compute the nonlinear transfer in the prognostic region and also to compute the integral quantities occurring in the dissipation source function. Tests with an f^{-5} tail indicated that the model was not sensitive to the precise form of the diagnostic tail. The contribution to the total energy from the diagnostic tail is normally negligible.

The model has been implemented and tested in regional versions with ¼° × ½° latitude–longitude res-

olution for the North Atlantic and the Gulf of Mexico and has been run globally with $3° \times 3°$ resolution.

The model is fully vectorized. In the deep-water mode, using the first-order propagation scheme, the model requires about 5 sec CPU-time per time step on a single processor CRAY-XMP or a CYBER 205. For the global $3° \times 3°$ grid, this corresponds to 6 CPU-minutes per model day integration for a 20 minute (source function) integration time step. The shallow water mode requires about 40% more computer time.

3. Extension to shallow water

To generalize the deep-water transport equation (2.1) to shallow water, the source function (2.7) needs to be extended to include an additional source function S_{bf} representing the energy loss due to bottom friction and percolation. The other terms of the transport equation must also be suitably modified to allow for the dependence on the depth D of the finite depth dispersion relation

$$\omega = (gk \tanh kD)^{1/2}. \qquad (3.1)$$

Specifically, the following changes were made:

- The additional bottom friction term was taken from the JONSWAP Study (Hasselmann et al. 1973)

$$S_{bf} = -\frac{\Gamma}{g^2} \frac{\omega^2}{\sinh^2 kD} F \qquad (3.2)$$

with $\Gamma = $ constant $= 0.038$ m^2 s^{-3}.
- The infinite depth group velocity $v = \frac{1}{2}\omega/k$ in the propagation equations (2.2)–(2.4) was replaced by the corresponding expression for finite depth D,

$$v = \frac{\partial \omega}{\partial k} = \frac{1}{2}\left(\frac{g}{k}\tanh kD\right)^{1/2}\left(1 + \frac{2kD}{\sinh 2kD}\right). \qquad (3.3)$$

- In the expression (2.9) for the wind input β factor, the phase velocity c in the term (u_*/c) was replaced by the appropriate value for finite depth.
- Assuming that the white capping dissipation is controlled primarily by the wave slope, the source function S_{ds} was rewritten in terms of wavenumbers rather than frequencies (except for a residual factor ω providing the dimension needed for a time derivative),

$$S_{ds} = -(2.36 \cdot 10^{-5})\tilde{\omega}\left(\frac{k}{\tilde{k}}\right)\left(\frac{\tilde{\alpha}}{\tilde{\alpha}_{PM}}\right)^2 F \qquad (3.4)$$

where

$$\tilde{k} = \left(E^{-1}\int F(k)k^{-1/2}dk\right)^{-2} \qquad (3.5)$$

$$\tilde{\alpha} = E\tilde{k}^2 \quad (\tilde{\alpha} \rightarrow \bar{\alpha} \text{ for } \tilde{k}D \rightarrow \infty). \qquad (3.6)$$

- On the basis of the exact numerical computations of Hasselmann and Hasselmann (1981), the nonlinear transfer for finite depth was taken as identical to the

deep water transfer rate for a given frequency-direction spectrum, except for a scaling factor R,

$$S_{nl}(\text{finite depth}) = R(kD)S_{nl}(\text{deep water}). \qquad (3.7)$$

The exact computations could be closely reproduced in the range $kD > 1.0$, for which the simple scaling relation (3.7) is applicable using the scaling factor

$$R(x) = 1 + \frac{5.5}{x}\left(1 - \frac{5x}{6}\right)\exp\left(-\frac{5x}{4}\right). \qquad (3.8)$$

- Following the dimensional arguments of Zakharov and Zaslavskiy (1982), Kitaigorodskii (1983) and others, the f^{-4} high-frequency tail defined by (2.22) was replaced by the expression

$$F(f, \theta) = \left(\frac{v_{hf}}{v}\right)\left(\frac{k}{k_{hf}}\right)^{-2.5} F(f_{hf}, \theta) \quad \text{for} \quad f > f_{hf}. \qquad (3.9)$$

This is identical to (2.16) for deep water but yields a wavenumber rather than frequency power law for finite depth waves (the one-dimensional wavenumber spectrum becomes proportional to $k^{-2.5}$).

- The great circle refraction term (2.4) [denoted in (3.10) by $\dot{\theta}_{gc}$] was augmented to include the refraction $\dot{\theta}_D$ due to variations of the water depth (cf. Phillips 1977),

$$\dot{\theta} = \dot{\theta}_{gc} + \dot{\theta}_D \qquad (3.10)$$

where

$$\dot{\theta}_D = \frac{1}{kR}\frac{\partial \omega}{\partial D}\left(\sin\theta \frac{\partial D}{\partial \phi} - \frac{\cos\theta}{\cos\phi}\frac{\partial D}{\partial \lambda}\right). \qquad (3.11)$$

In the finite depth WHIST hindcast studies presented in section 6, however, the depth-dependent angular refraction term (3.11) was generally ignored, although the shoaling effect, i.e., the depth dependence of v in Eq. (3.3), was retained. This was based on the finding in JONSWAP and other studies that on larger scales finite depth angular refraction is generally dominated by statistical subgrid-scale refractive scattering ("scintillation") rather than by deterministic large-scale ray bending. In one WHIST hindcast test, the depth-dependent angular refraction was included (Gao 1986), and the effect of the deterministic large-scale ray bending was indeed found to be quite small. A realistic treatment of refractive scattering effects on the scales of these hindcasts requires either a higher resolution grid and bottom topography than was available for these studies or a separate statistical treatment.

For more extensive applications of the shallow water model to particular geographical regions, it will probably be necessary to tune the bottom friction source function (3.2), which was appropriate for the JONSWAP site, to the locally varying bottom conditions (sand grain size, influence of percolation, interaction with local currents, etc., of Shemdin et al. 1978). How-

ever, the provision of a shallow water version of the third generation model, even in the present general form, was regarded as a high priority item in the development of the model, since the inherent spectral shape restrictions of second generation models cannot be readily justified for shallow-water waves. The first-order equilibrium and scaling arguments put forward for deep-water waves (Hasselmann et al. 1976) do not carry over to the shallow water case (cf. the SWIM Group 1985).

4. Numerical implementation

Different numerical techniques and time steps were used to integrate the source functions and the advective terms of the transport equation.

a. Implicit integration of the source functions

An implicit scheme was introduced for the source function integration to enable the use of an integration time step that was greater than the dynamic adjustment time of the highest frequencies still treated prognostically in the model. In contrast to first and second generation wave models, the energy balance of the spectrum is evaluated in detail in the present model up to a high cutoff frequency. The high-frequency adjustment time scales are considerably shorter than the evolution time scales of the energy-containing frequency bands near the peak of the spectrum, in which one is mainly interested in modeling applications. Thus, in the high-frequency region, it is sufficient to determine the quasi-equilibrium level to which the spectrum adjusts in response to the more slowly changing low-frequency waves, rather than the time history of the short time-scale adjustment process itself. A time-centered implicit integration scheme whose time step is matched to the evolution of the lower frequency waves meets this requirement automatically: for low-frequency waves, the integration method yields essentially the same results as a simple forward integration technique (but is of second rather than first order), while for high frequencies the method yields the (slowly changing) quasi-equilibrium spectrum.

The implicit second-order, centered difference equations (leaving out the advection terms) are given by

$$F_{n+1} = F_n + \frac{\Delta t}{2}(S_{n+1} + S_n) \qquad (4.1)$$

where Δt is the time step and the index n refers to the time level.

If S_{n+1} depends linearly on F_{n+1}, Eq. (4.1) could be solved directly for the spectrum F_{n+1} at the new time step. Unfortunately, only the input source function is linear. For this term we write

$$S_{n+1}^{in} = \beta_{n+1}F_{n+1} = \beta_{n+1}\Delta F + \beta_{n+1}F_n \qquad (4.2)$$

where

$$\beta_{n+1} = \beta(u_*^{n+1}), \qquad (4.3)$$

$$\Delta F = F_{n+1} - F_n. \qquad (4.4)$$

For the remaining source function

$$S_{n+1}^{rest} = S_{n+1}^{nl} + S_{n+1}^{ds}, \qquad (4.5)$$

we introduce a Taylor expansion

$$S_{n+1}^{rest} = S_n^{rest} + \frac{\partial S_n^{rest}}{\partial F}\Delta F + \cdots. \qquad (4.6)$$

The functional derivative in (4.6) (numerically, a discrete matrix M_n) can be divided into a diagonal matrix Λ_n and a nondiagonal residual N_n,

$$\frac{\partial S_n^{rest}}{\partial F} \equiv M_n = \Lambda_n + N_n. \qquad (4.7)$$

Substituting (4.2), (4.6), and (4.7) into (4.1), we obtain

$$\left[1 - \frac{\Delta t}{2}(\Lambda_n + N_n + \beta_{n+1})\right]\Delta F$$
$$= \Delta t\left[\left(\frac{\beta_n + \beta_{n+1}}{2}\right)F_n + S_n^{rest}\right]. \qquad (4.8)$$

If the nondiagonal terms are not too large, the matrix on the left-hand side can be inverted by expanding with respect to the nondiagonal contributions, yielding

$$\Delta F(f, \theta) = A(f, \theta)$$
$$+ \sum_{f',\theta'} B(f, \theta; f', \theta')A(f', \theta') + \cdots, \qquad (4.9)$$

where the diagonal term is given by

$$A(f, \theta) = \left\{\left[\Delta t\frac{(\beta_n + \beta_{n+1})}{2}F_n + S_n^{rest}\right]\right.$$
$$\left.\times\left[1 - \frac{\Delta t}{2}(\Lambda_n + \beta_{n+1})\right]^{-1}\right\}_{(f,\theta)} \qquad (4.10)$$

and the first nondiagonal matrix in the expansion takes the form

$$B(f, \theta; f', \theta') = \frac{N_n(f, \theta; f', \theta')\frac{\Delta t}{2}}{\left\{1 - \frac{\Delta t}{2}(\Lambda_n + \beta_{n+1})\right\}_{(f,\theta)}}. \qquad (4.11)$$

The matrix M_n can be readily determined in the course of computing the source functions S_n^{nl} and S_n^{ds}. The inclusion of the diagonal contributions (4.10) then requires little more computing time per time step than an explicit scheme. Significantly more calculations are involved, however, in the evaluation of the nondiagonal contributions. Fortunately, a number of trial computations indicated that the off-diagonal contributions

were generally small if the time step was not too large. For a typical test case, good agreement was obtained between an explicit integration with a time step of 3 minutes and the implicit scheme with only diagonal terms for time steps up to about 20 minutes.

b. Propagation

Two alternative propagation schemes were implemented in the model: a first-order upwind scheme

$$F_j^{n+1} = F_j^n - \sum_k \frac{\Delta t}{\Delta x_k \cos\theta_j} [(u \cos\phi F^n)_j$$

$$- (u \cos\phi F^n)_{k_-}] \quad (4.12)$$

and a second order leapfrog scheme

$$F_j^{n+1} = F_j^{n-1} - \sum_k \frac{\Delta t}{2\Delta x_k \cos\phi_j} [(u \cos\phi F^n)_{k_+}$$

$$- (u \cos\phi F^n)_{k_-}] + \text{diffusion.} \quad (4.13)$$

In equations (4.12), (4.13) the index n refers to the time level and the indices k_-, k_+ to the neighboring grid points in the upstream and downstream propagation directions, respectively, relative to the reference grid point j. The index k runs over the three propagation directions λ, ϕ and θ, and u_k, Δx_k denote the velocity component (λ, ϕ, θ) and grid spacing, respectively, in the relevant direction.

The first-order scheme is characterized by a higher numerical dispersion, with an effective diffusion coefficient $D \sim \Delta x^2 / \Delta t$. For numerical stability, the time step must satisfy the inequality $\Delta t < \Delta x / v$, so that $D > \Delta x v$. The advection term of the second-order scheme has a smaller inherent numerical dispersion, but suffers from the drawback that it generates unphysical negative energies in regions of sharp gradients. This can be alleviated by including explicit diffusion terms, as indicated in Eq. (4.13). In practice, the explicit diffusion required to remove the negative side lobes in (4.13) is of the same order as the implicit numerical diffusion in (4.12), so that the effective dispersion is generally comparable for both schemes. The details of the diffusion scheme are given in appendix B.

Figures 1 and 2 show examples of the propagation and dispersion of wave packets along various great cir-
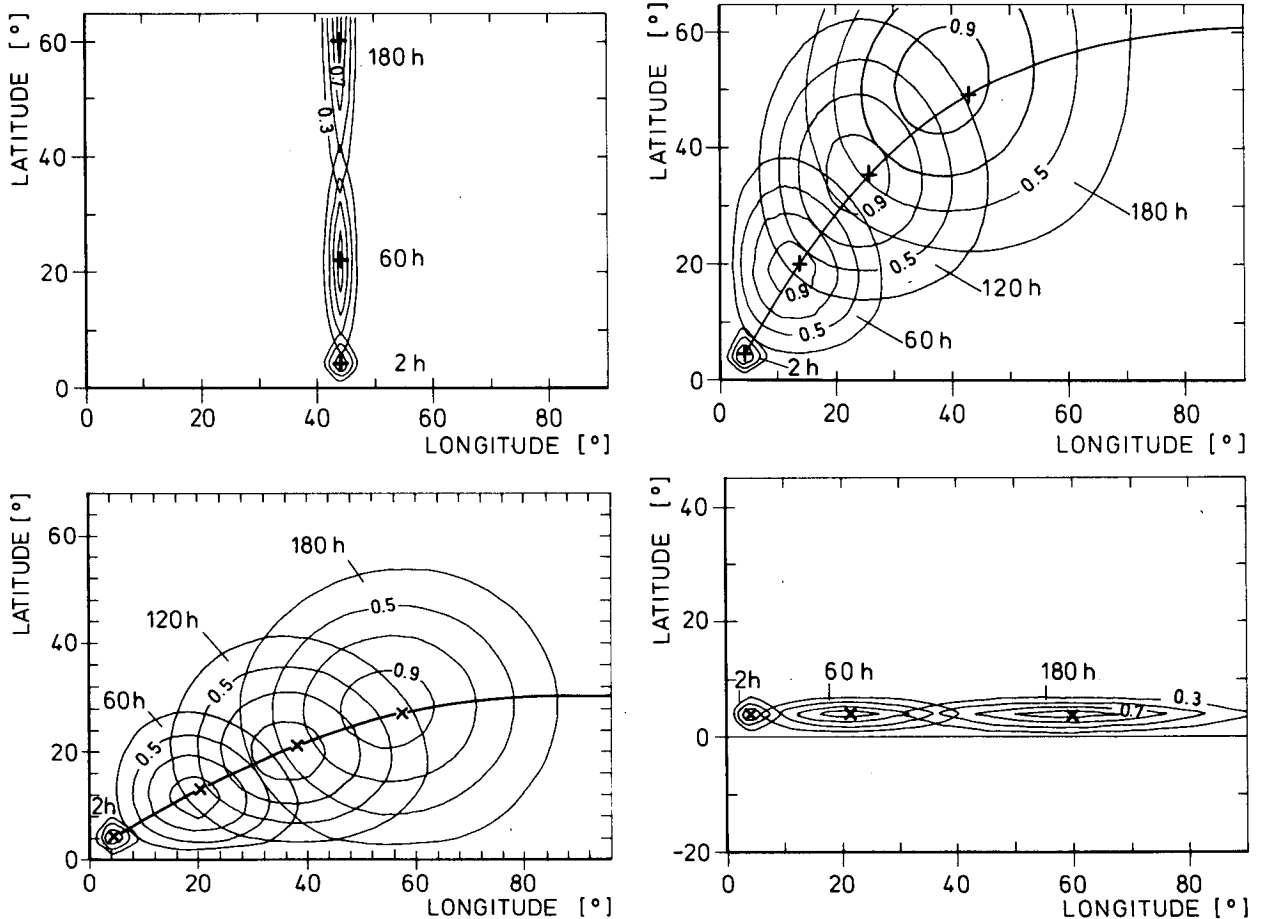

FIG. 1. Propagation of wave packets along various great circle paths for an initial δ-function pulse for first-order propagation scheme. Crosses mark theoretical position of a nondispersed pulse.
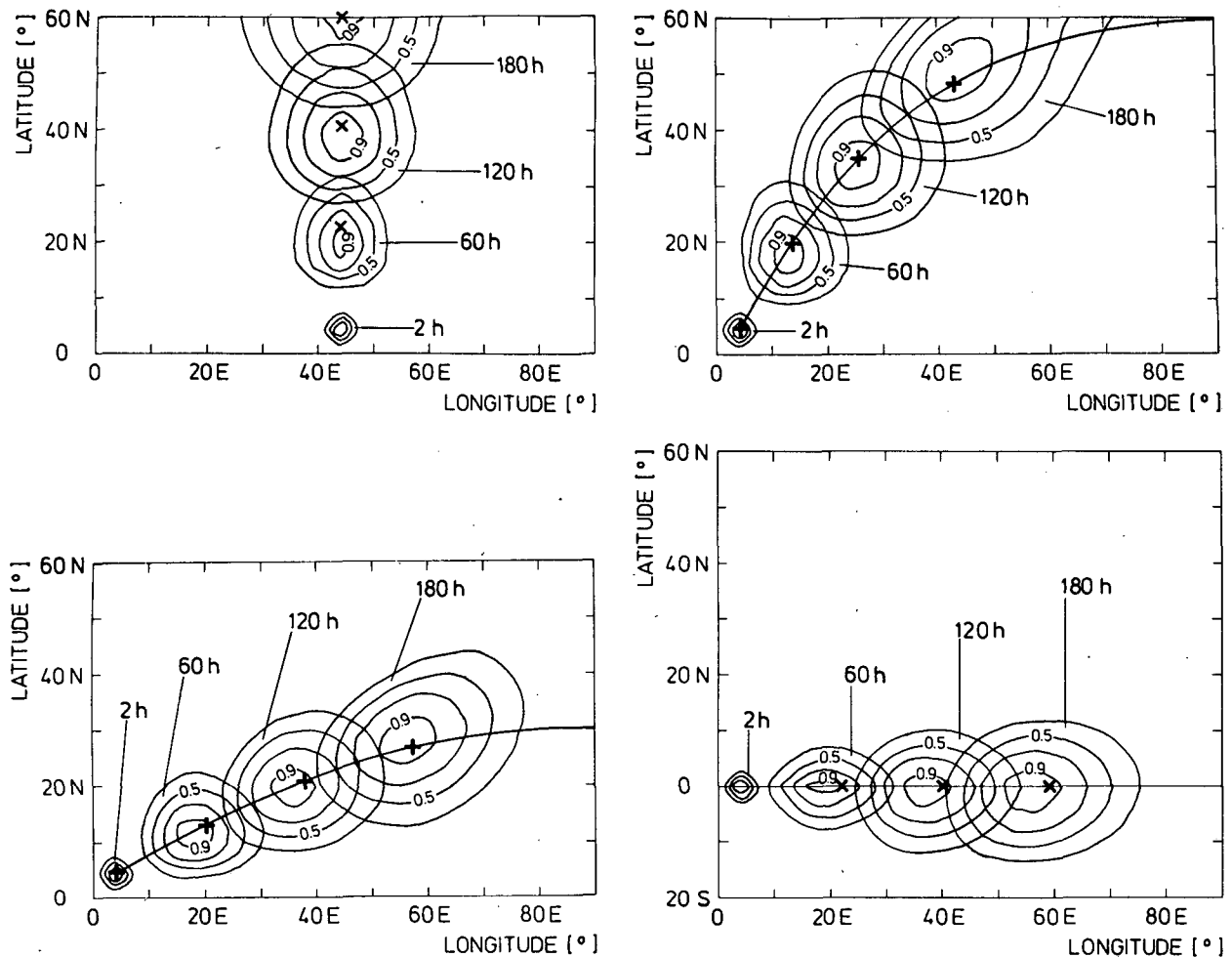
FIG. 2. As in Fig. 1 but for a second-order propagation scheme with additional explicit diffusion (cf. appendix B for details).

cle paths for the first and second order propagation schemes. The initial distributions were δ-functions (i.e., concentrated within a single grid cell with respect to λ, φ and θ). The Courant number (at the equator) was set as $v\Delta t/\Delta x = v\Delta t/R\Delta\phi = 0.16$ (a rather low Courant number for typical wave frequencies is unavoidable in wave models in order to remain within the stability limit for the lowest frequencies). The mean propagation and dispersion properties are similar for both schemes and are in order of magnitude agreement with the dispersion appropriate for the present wave model with a frequency resolution $\Delta f/f = 0.1$ and an angular resolution $\Delta\theta = 30°$. An advantage of the second-order scheme is that the lateral dispersion is less dependent on the propagation direction than in the first order scheme, which shows significant differences in the dispersion characteristics for waves traveling due north–south or east–west compared with directions in between.

The main motivation for considering the second-order scheme in addition to the first-order scheme was

not to reduce the dispersion, but to be able to control it. In contrast to most other numerical advection problems, an optimal propagation scheme for a spectral wave model is not designed to minimize the numerical dispersion, but rather to match it to the finite dispersion associated with the finite frequency-direction spectral resolution of the model (SWAMP, appendix B, 1985). The dispersion due to the different propagation velocities of the different wave components within a finite frequency–directional bin increases linearly with respect to propagation time or distance, whereas most propagation schemes yield a spreading of the wave groups, which increases at the root of the propagation time or distance. However, it has been shown by Booij and Holthuijsen (1987) that linear spreading rates can be achieved by introducing a variable diffusion coefficient proportional to the "wave age." Although this has not yet been implemented, the second-order scheme with explicit diffusion provides a framework for testing the Booij–Holthuijsen method.

All results presented in this paper were obtained with

the upwind first-order scheme (4.12). In general, the differences between the model results using the first- or second-order propagation methods were small.

5. Fetch-limited wave growth

Figures 3 and 4 show the growth of the nondimensional wave energy $E^* = Eg^2/u_*^4$ and peak frequency $f_p^* = f_p u_*/g$ as a function of fetch for the case of a uniform wind blowing orthogonally offshore for deep water waves. Also shown are the growth curve bands for the JONSWAP data and various wave models investigated in the SWAMP (1985) Study.

The corresponding growth curves for the one-dimensional frequency spectrum are shown in Fig. 5. An overshoot is present but is somewhat less pronounced than in the corresponding simulations with a model in which the nonlinear transfer integral was computed exactly (cf. Hasselmann and Hasselmann, chapter 24 in SWAMP 1985). This presumably represents a shortcoming of the discrete interaction approximation of the nonlinear transfer.

Figure 6 shows the angular spread parameter s for the fully developed spectrum, where s is determined by a least-squares fit of the directional distribution $[E(f, \theta)/E(f)]$ to the model directional distribution

$$S = N(s) \cos^{2s}\left(\frac{\theta - \bar{\theta}}{2}\right) \qquad (5.1)$$

and $N(s)$ is a normalization constant. The frequency dependence of s agrees remarkably well with the form derived by Hasselmann et al. (1980) from directional buoys.
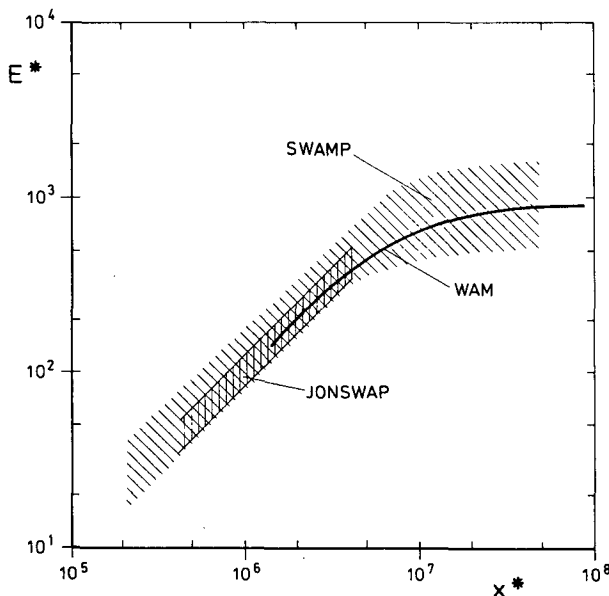
FIG. 3. Wave energy as a function of fetch for uniform wind, fetch-limited wave growth. Also shown are growth curve bands for JONSWAP and various first and second generation wave models (from SWAMP 1985).
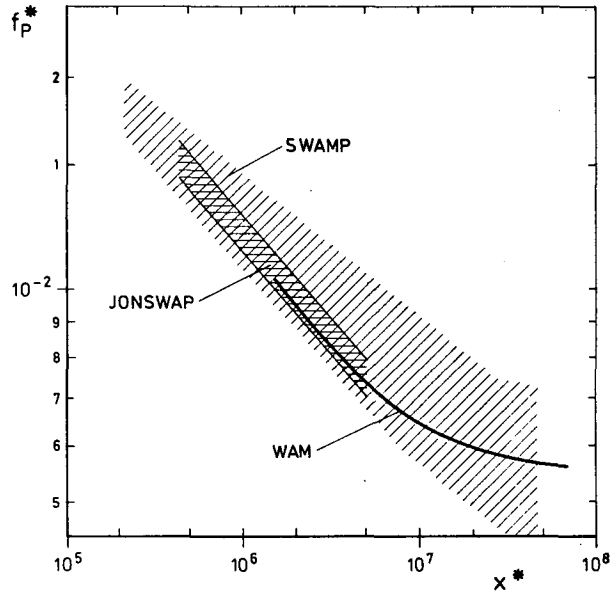
FIG. 4. As in Fig. 3 but for the peak frequency.

The growth curves for the finite (uniform) depth case are shown in Figs. 7 and 8. The effect of the additional bottom friction source function is to restrict the development of the long waves ($kD \leqslant 1.0$). The $\sinh^2 kD$ factor in (3.2) acts as a very sharp, low-frequency cutoff filter.

In Fig. 9 a comparison is made with results from various second generation models (BMO, GONO and HYPA), which were compared in the SWIM project, (the SWIM Group 1985), and with a recent simulation by a one-dimensional model (NL shallow) in which the nonlinear transfer was computed by complete numerical integration of the Boltzmann integral (Weber 1988). The quantity selected for the comparison in Fig. 9a is $E_*^\infty(D_*)/E_*^\infty(\infty)$, where E_*^∞ is the total dimensionless variance obtained at the largest fetch considered and $D_* = Dg/u_*^2$. It is known that different second generation finite depth models exhibit rather different fetch growth properties, and this is well illustrated by the figure. (One should bear in mind, however, that a flat, shallow bottom and infinite fetch seldom occur in practice.) The results of the WAM model lie more or less in the middle and are close to the results of the "exact" one-dimensional model, NL shallow. Figure 9b shows the effect of depth limitation on the frequency. For the WAM model the mean frequency has been considered; for the other models the peak frequency has been taken. In either case, the ratio of the depth-limited value at infinite fetch to the corresponding deep water value is shown, for which the choice of peak or mean frequency is not so critical. The resulting picture is the same as in Fig. 9a: fairly large differences between different second generation models, with the WAM curve lying somewhere in the middle.
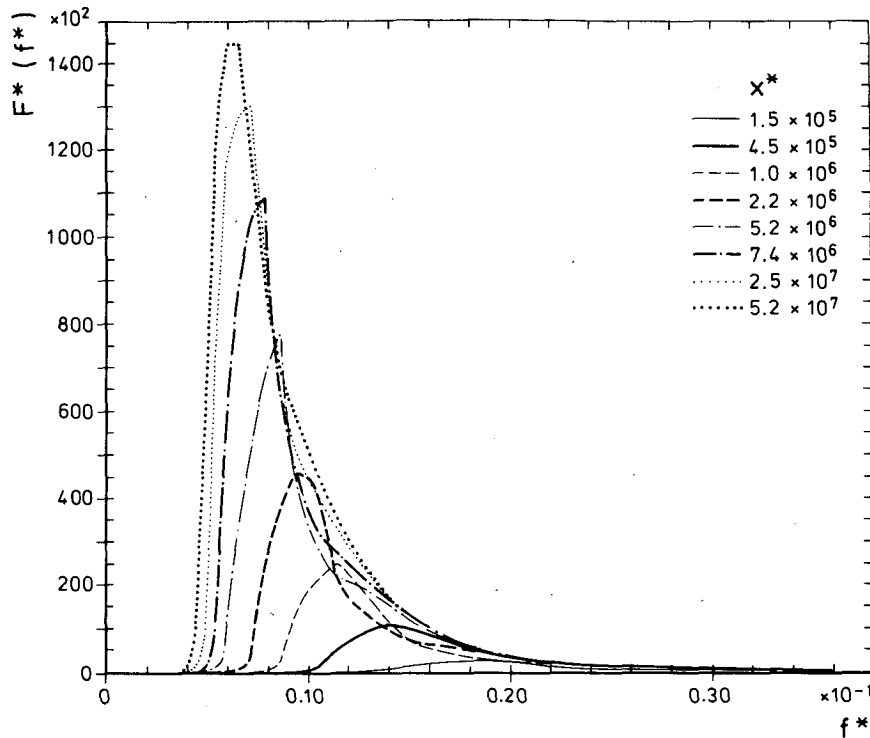
FIG. 5. Evolution of one-dimensional frequency spectrum for fetch-limited wave growth.

After the model had been tuned to simulate satisfactorily the standard infinite-depth, fetch-limited growth case and had been extended to finite depth, the model was applied without further adjustments to a series of hindcast cases involving strongly variable wind fields. These provided a test of the model for complex wave spectra, which were strongly influenced by directional relaxation processes, cross-spectral interactions, and pronounced spatial inhomogeneities.

FIG. 6. Directional spreading parameter for a fully developed spectrum.

6. Six hindcast studies of North Atlantic–North Sea (WHIST) storms

In preparation for an extensive hindcast study to compile wave statistics for the North Atlantic and North Sea over a 20-year period (the NESS project), wind fields for six storms characteristic for this region were analyzed by Francis et al. (1985). The wave fields for all six storms were computed using the shallow water, first-order propagation model and compared against wave measurements taken at 11 stations in the North Sea. Tables 1 and 2 give listings of the storms and station positions, respectively.

All runs were performed on a fine mesh, $\frac{1}{4}°$ latitude, $\frac{1}{2}°$ longitude grid covering part of the North Atlantic, the Norwegian Sea, and the North Sea. The propagation time step was set at 15 minutes, within the stability limits of the first order, upwind advection scheme.

The wind fields for the storms were kindly provided by the Meteorological Office in Bracknell (BMO). The wind speed U was transformed to friction velocity fields u_* according to

$$u_* = U\sqrt{C_D(U)}$$

where the drag coefficient $C_D(U) = C_D(U_{10})$ is given by

$$C_D(U) = \begin{cases} 1.2875 \ 10^{-3}, & U < 7.5 \text{ m s}^{-1} \\ (0.8 + 0.065U) 10^{-3}, & U \geq 7.5 \text{ m s}^{-1}. \end{cases}$$

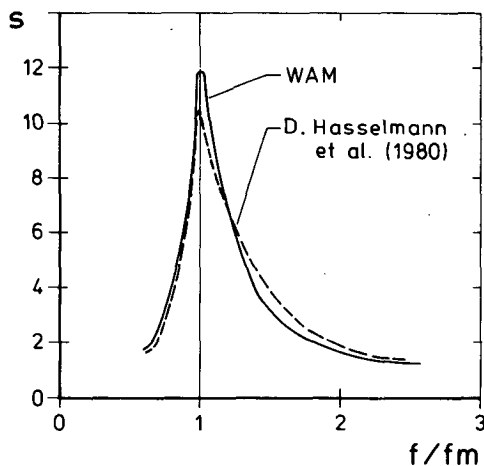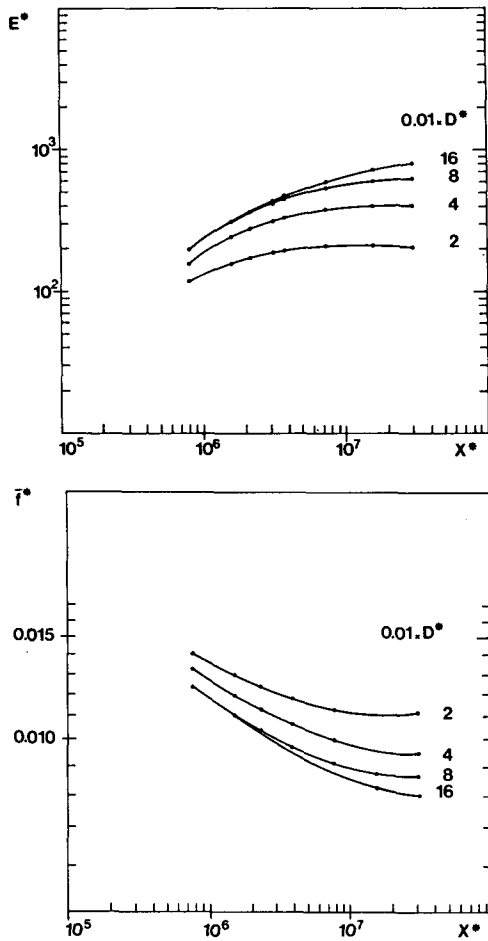FIG. 7. (a) Wave energy as a function of fetch for fetch-limited wave growth on water of constant finite dimensionless depth D^* = Dg/u_*^2. (b) As in (a) but for mean frequency.

This choice of the expression for the drag coefficient was found to be crucial in resolving some remarkable differences between wave growth datasets collected in the North Sea (Janssen et al. 1987). No further corrections, for example for atmospheric stability, were applied.

The results of only two storms are discussed here briefly. A more complete account of the results may be found in Bertotti et al. (1986).

The first storm, storm 1, occurred in the period 3-4 January 1983. A low center moved northeast during 3 January from (58°N, 12°W) at midnight to (65°N, 0°E) 24 hours later. The associated wind fields affected the central and northern areas of the North Sea, being southerly at first and then veering to southwesterly. Maximum wind speeds were around 25 m s^{-1} at northern platforms. At the location of the buoys off central Norway (Haltenbanken and Traenebanken) the winds backed as the depression approached, maximum strengths reaching about 20 m s^{-1} at midnight on 4 January. As an example, the wind field for storm 1 at

0600 UTC 4 January 1983 is shown in Fig. 10. This figure also shows a map of the stations, the model region, and the grid.

The significant wave heights and mean propagation directions of the wave field for this time are shown in Fig. 11 as a Custer diagram (a field of vectors whose length is proportional to the wave height pointing in the mean wave propagation direction) with superimposed wave height isolines.

The wave height and direction fields provide only a general picture of mean wave field properties, without information on the detailed two-dimensional frequency and directional distribution of the local wave spectrum. An indication of the evolution of the full two-dimensional spectrum is given by the series of spectra for the station Statfjord (Fig. 12) for storm 1 on 3–4 January 1983. The wave field is clearly nonstationary, with rapidly changing directional distributions. The energy gap between the northward and eastward propagation directions, which is evident in several panels (e.g., 4 January at 0600 UTC), may be attributed to sheltering by the Shetland Islands. The sheltering effects of islands can also be clearly seen in the wave height map, Fig. 11.

In general, the model performed well, especially for the stations in the southern and central part of the North Sea, as may be inferred from the time series in Fig. 13. At the northern stations Utsira, Brent, and
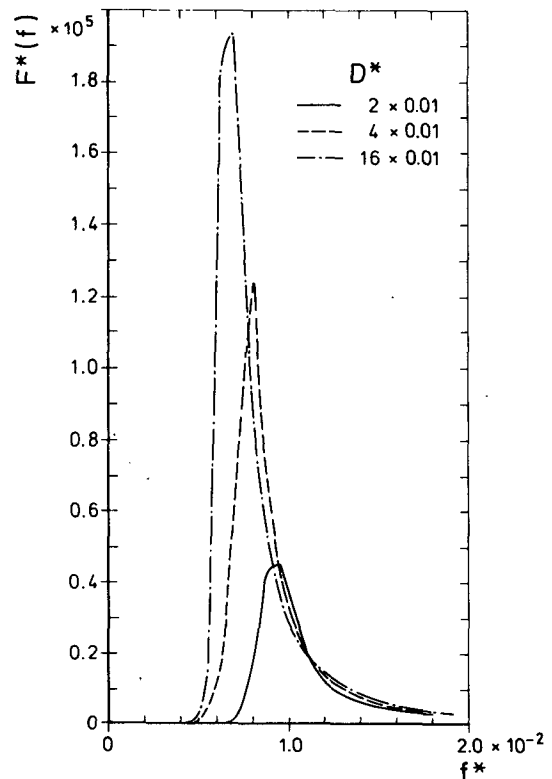

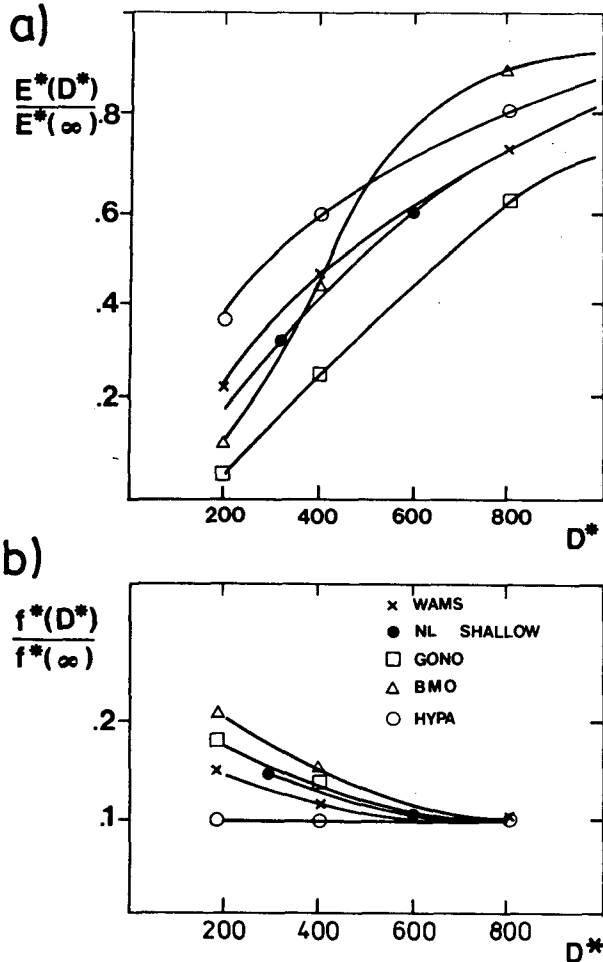FIG. 8. Fully developed finite depth frequency spectrum for different values of D_*.

FIG. 9. (a) $E^{\infty}(D_*)/E^{\infty}(\infty)$ as a function of D_*, for five different models, where $E^{\infty}(D_*)$ is the total dimensionless variance at dimensionless depth D_* and at the largest fetch considered. (b) $f^{\infty}(D_*)/f^{\infty}(\infty)$ as a function of D_* for five different models. Here $f^{\infty}(D_*)$ denotes the mean frequency for the WAM model and the peak frequency for the other models. In both cases $f^{\infty}(D_*)$ refers to the value obtained for finite depth at the largest fetch considered.

Statfjord, an underestimate of the peak wave heights is found. Inspection of the isoline map in Fig. 11 indicates that, due to the presence of the Shetlands, a considerable sheltering occurs in this region. Possibly the gap between the Shetlands is represented as too narrow in the model grid, resulting in too much sheltering.

TABLE 1. WHIST storms.

Storm	Date
1	3–4 January 1983
2	6–7 January 1983
3	9–10 January 1983
4	18–19 January 1983
5	1–2 February 1983
6	1–4 January 1984

TABLE 2. Stations used for WHIST hindcast verification. Source key: KNMI, Royal Netherlands Meteorological Institute; IKU, Continental Shelf Institute; DHI, German Hydrographic Institute; and NH, Norsk Hydro.

Name		Position	Source
01. Euro	O	52.0°N, 3.6°E	KNMI
02. Ijmuiden	I	52.6°N, 4.1°E	KNMI
03. K-13	K	53.2°N, 3.2°E	KNMI/Shell
04. FPN	F	54.7°N, 7.2°E	DHI
05. Ekofisk	E	56.5°N, 3.2°E	NH
06. Utsira	U	59.3°N, 4.8°E	NH
07. Brent	B	61.0°N, 1.5°E	Shell
08. N. Cormorant	C	61.2°N, 1.2°E	Shell
09. Statfjord	S	61.3°N, 1.9°E	NH
10. Haltenbanken	H	65.0°N, 7.5°E	IKU
11. Traenebanken	T	66.3°N, 9.5°E	IKU

As a second storm, we consider storm 6 of the WHIST study, which occurred during the period 1–4 January 1984. Strong southwest winds (in the south) and west winds (in the north) prevailed over the North Sea during 1 and 2 January, arising from a low pressure area in the Norwegian Sea. A new depression moved rapidly from the south of Iceland at 1200 UTC 2 January, reaching the Skagerrak at midnight 4 January. The wind fields were generally very strong, especially in the south early on 3 January (20–25 m s^{-1} southwest, veering to west–southwest by 0600 UTC) and in the central North Sea around midday on 3 January (up to 30 m s^{-1} from the southwest). A complete veering to northwesterly had occurred in northern and central regions by midnight on 4 January, and in southern regions 6 hours later.

At the location of the Norwegian buoys, the model achieved a reasonable match for the peak values occurring on 2 January (cf. Fig. 14). The peak at the North Cormorant platform on 4 January is simulated rather well, and there is also a good agreement between the model and the measurement at Statfjord.

With respect to the peak values, the agreement between model and measurements is not so favorable for this period for Ekofisk and the southern station, except at Euro. However, as already noted by Francis et al. (1985), this may be due to missing local features in the analyzed wind fields in this region.

The results for the remaining storms are qualitatively similar. The overall agreement is generally quite good, as borne out also by the verification statistics for all six storms listed in Table 3. The results are particularly encouraging in view of the fact that no additional "tuning" of the WAM model was performed for these finite depth applications.

7. Hurricane cases

a. Test storms

In order to validate the WAM model against wave measurements obtained in complicated wave regimes under extreme wind forcing situations, complete hind-
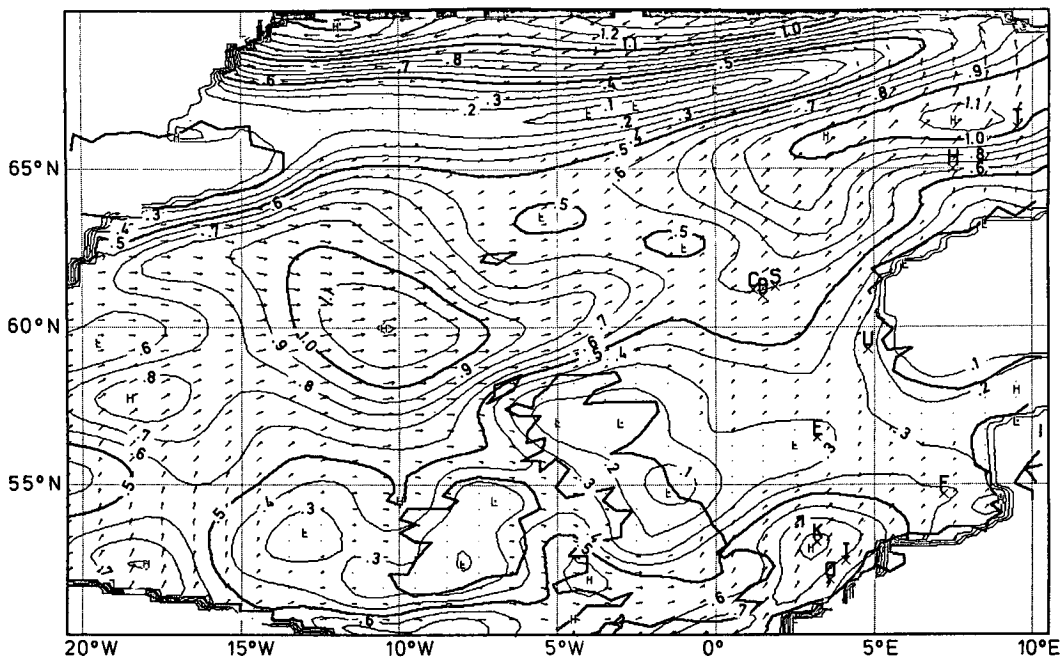
FIG. 10. Wind field for storm 1 at 0600 UTC 4 January 1983 plotted on the same grid as used by the model. Station positions listed in Table 2 are also indicated.

casts of the evolution of the wave field in three severe hurricanes were performed. All storms occurred in the Gulf of Mexico. Table 4 lists the storms and the corresponding measurement locations. The storm tracks for the storm periods modeled are shown in Fig. 15, which also displays the grid system used. The grid spacing is ¼° in latitude and longitude, which requires a propagation time step of 20 minutes. In all other respects (physics, spectral resolution, propagation) the wave model used is identical to that described above.
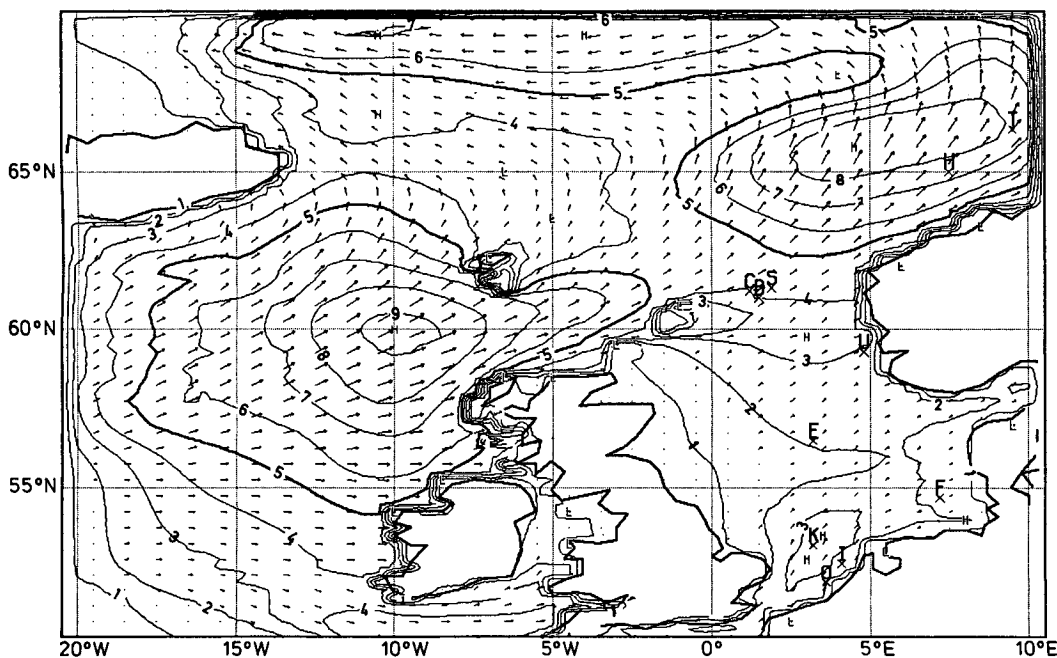
FIG. 11. Custer diagram and wave height isolines for wave field at 0600 UTC 4 January 1983.
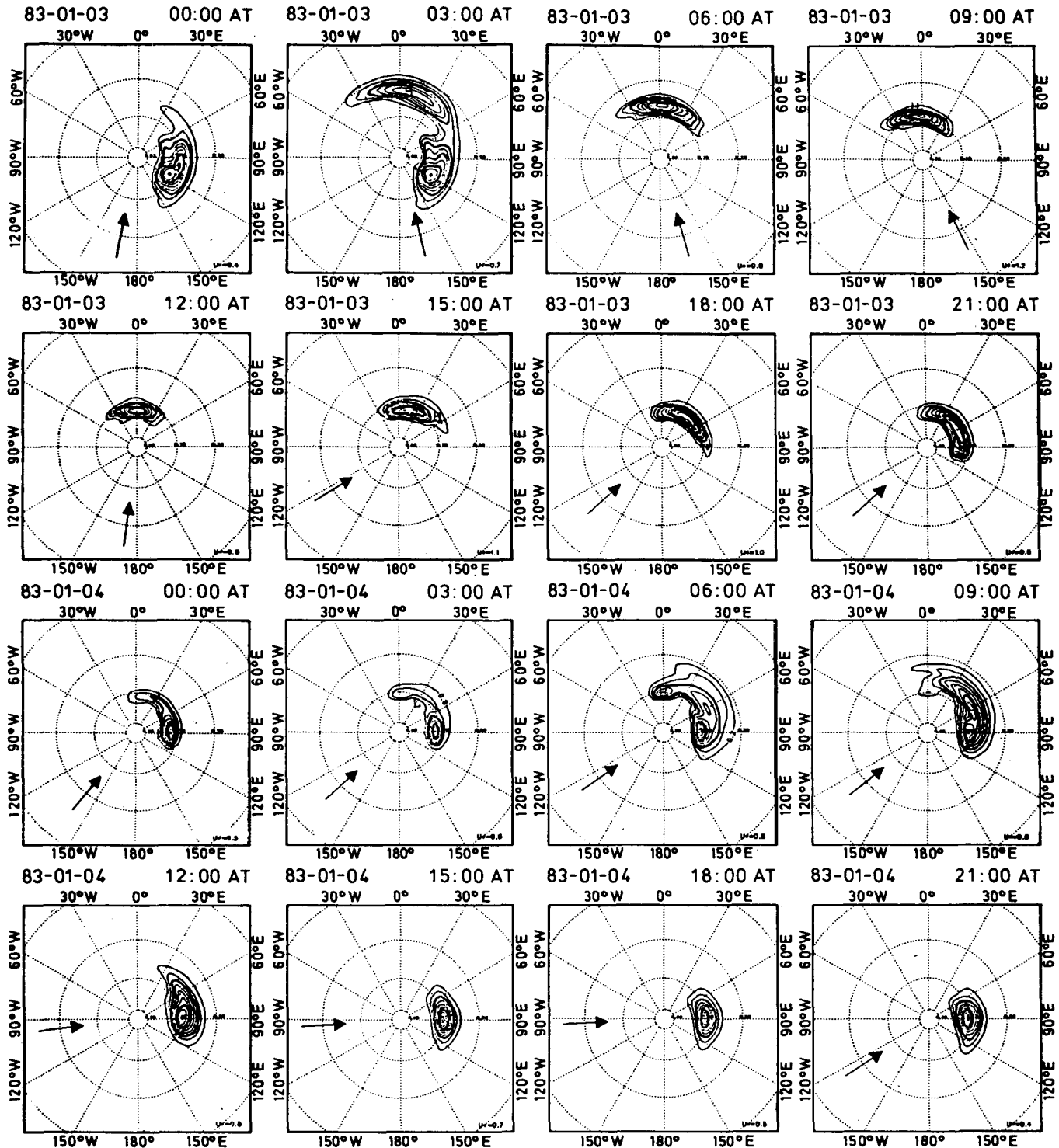
FIG. 12. Sequence of two-dimensional wave spectra at station Statfjord for storm 1.

b. Wave measurements

Table 4 lists the measurement sites (see also Fig. 15) and the types and sources of wave measurements used in this study. The wave measurements in Camille and Anita were made by capacitance type wave gauges mounted from production oil platforms. Significant wave heights and frequency spectra were estimated from wave records of 30 minutes in length.
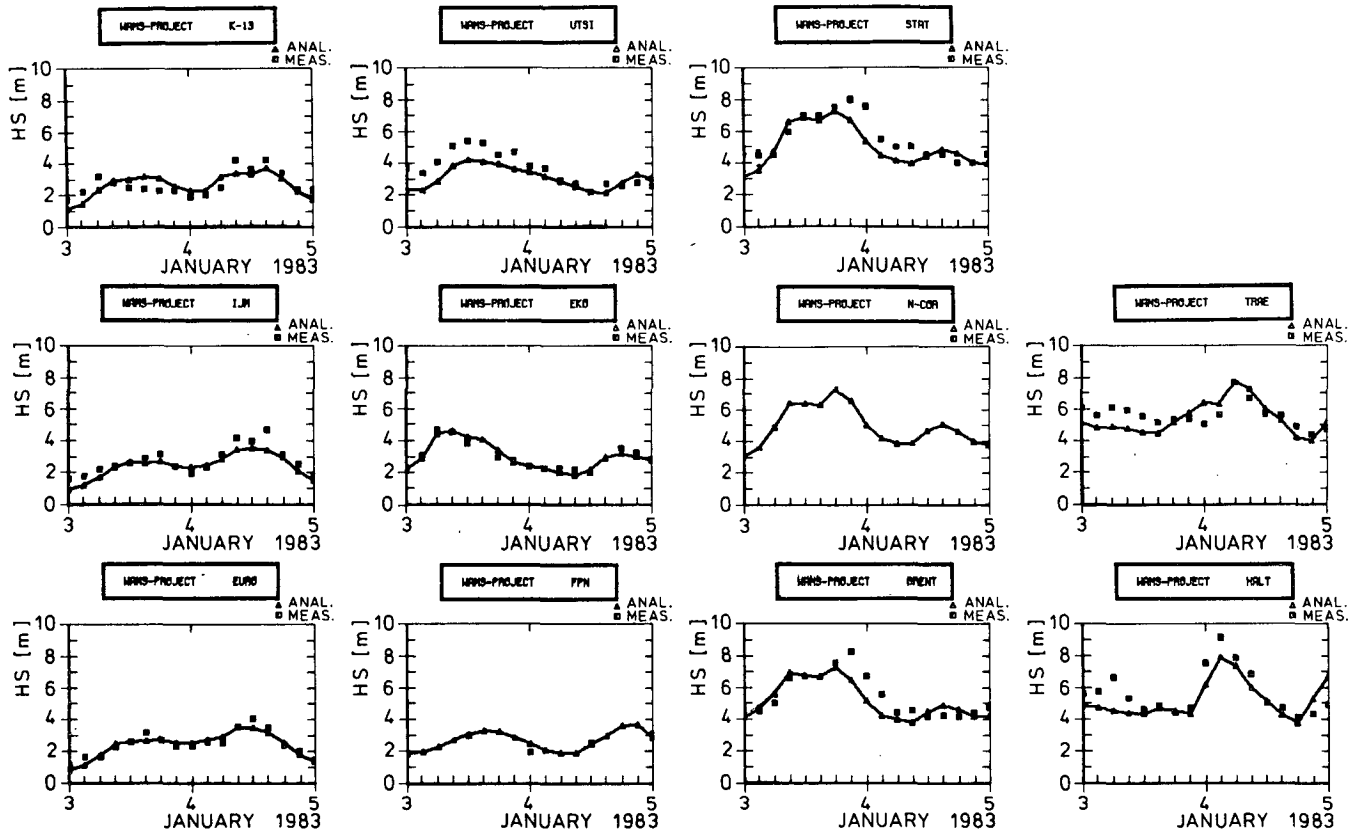
In hurricane Frederick at platform Cognac, located

FIG. 13. Hindcast and observed significant wave heights at the stations listed in Table 2 for WHIST storm 1.

in 312 m water depth, the measurement array consisted of a 30.5 m wave staff and two electromagnetic current meters positioned along a taut wire at depths of 21 and 6.7 m. Directional wave estimates were made following the method described by Forristall et al. (1978), in which cospectra between wave staff and top current meter channels were used to find the best estimates of the parameters $\bar{\theta}$ (mean direction of wave travel) and s (spreading parameter) in the function (5.1) as functions of wave frequency, where $N(s)$ is a normalizing factor. Comparisons between measurements and hindcasts in this storm at this site were restricted to frequency spectra and $\bar{\theta}(f)$. The latter were estimated from the hindcast two-dimensional spectra using a parabolic fit to the three largest values of the logarithm of the spectral density in each frequency band.

The rest of the wave data used in this study were provided by systems mounted in NOAA National Data Buoy Office (NDBO) moored buoys. Significant wave heights and spectra are processed on board from wave data sampled over a 20-minute period at three-hourly or hourly intervals. A complete description of the Wave Data Analyzers on the buoys is given by Steele et al. (1976).

For the record lengths used in the above measurement systems, the uncertainties in the significant wave height are about plus or minus 10 to 15 percent at the 90-percent confidence level (e.g., see Donelan and Pierson 1983). Also, estimates of the peak frequency are uncertain to plus or minus 5 percent, and the spectral density of the peak of the spectrum is generally overestimated.

c. Wind field specification

Hurricane wind fields were derived from application of a theoretical model of the horizontal air flow in the boundary layer of a moving vortex (Cardone et al. 1976). The model solves by numerical integration on a nested grid the vertically averaged equations of motion that govern a boundary layer subject to horizontal and vertical shear stresses.

The vertical shear stress is specified through a surface drag formulation (Cardone et al. 1979) based upon a similarity boundary layer parameterization, which incorporates a Charnock-type roughness specification. The model output can therefore be expressed in terms of the wind direction and wind speed at any desired reference level within the surface layer (e.g., 10 m) and the equivalent friction velocity.

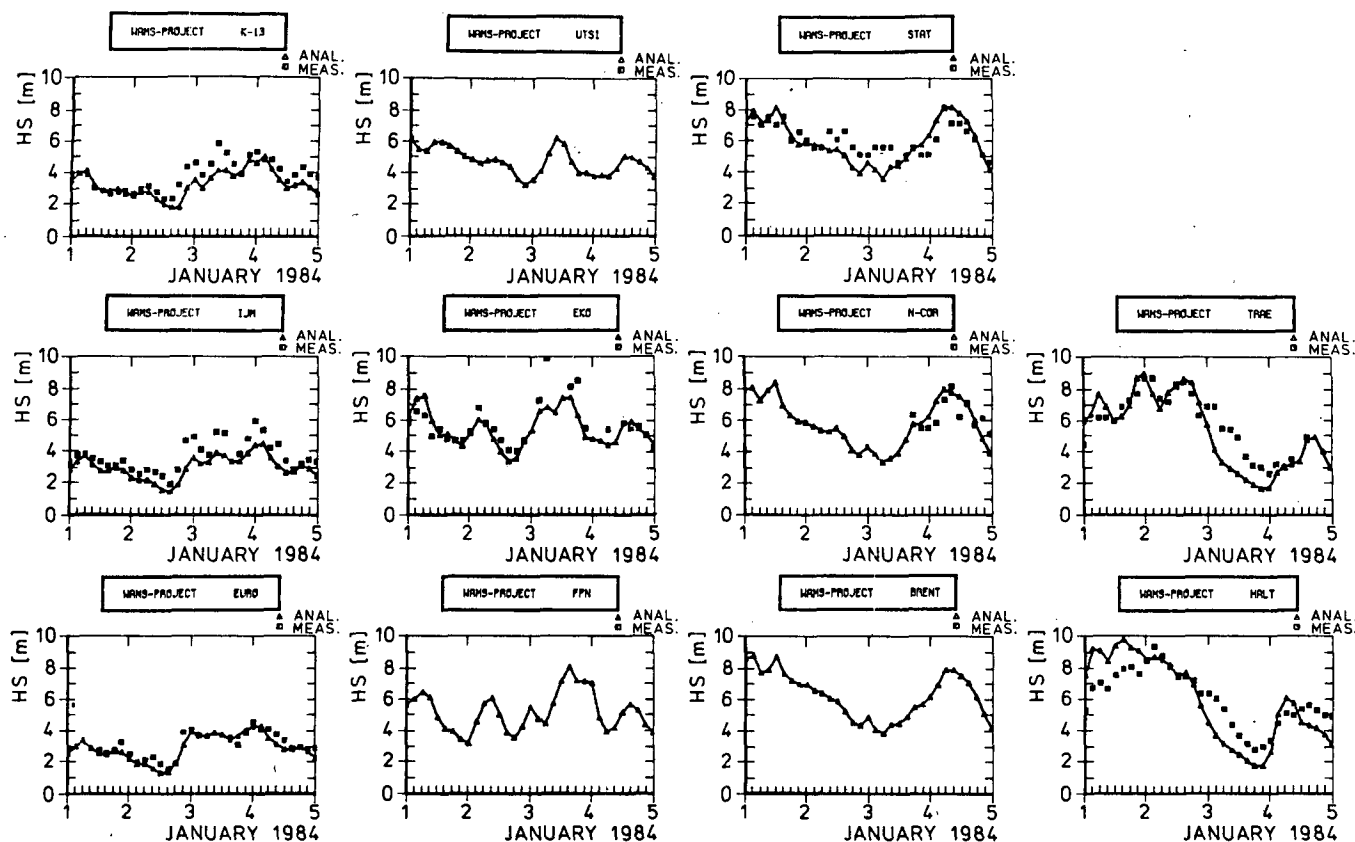The model pressure field is described as the sum of an axially symmetric part (p) and a large-scale pressure

FIG. 14. As in Fig. 13 but for WHIST storm 6.

field (p) of constant gradient. The symmetric part is described in terms of an exponential pressure profile

$$p = p_0 + \Delta p e^{-r_a/r}$$

where p_0 is the central pressure, Δp the storm pressure anomaly, and the r_a scaling radius nearly equivalent to the radius of maximum wind. The model can therefore be initialized from parameters that are usually available from historical meteorological records: Δp, r_a, v_f, and the ambient pressure field, p. The entire wind field history is computed from knowledge of the variation of those parameters along the storm track.

The model has been applied to nearly every major storm to affect the U.S. offshore area. Comparisons with overwater measurements from buoy and rigs sup-

TABLE 3. Mean observed wave heights, WAM model H_S^{bias} and scatter index (standard deviation/mean) for typical shallow water stations (EURO, IJMUIDEN, K13), and deep water station (EKOFISK, BRENT, STATFJORD) in the North Sea, for a hindcast of six WHIST storms.

Station	H_S^{obs} (m)	H_S^{bias} (m)	SI (%)
EURO, IJMUIDEN, K13,	3.2	0.16	16
EKOFISK, BRENT, STATFJORD	5.5	0.30	15

port an accuracy specification of plus or minus 20 degrees in direction and plus or minus 2 m s^{-1} in wind speed (1-hour average at 20-m elevation). Most comparisons have been published (e.g., see Cardone et al. 1976, 1978; Ross and Cardone 1978; Cardone and Ross 1979; Forristall et al. 1977, 1978, 1980).

The method provides winds to the wave model at half-hourly intervals. The winds are specified on the wave grid through bilinear interpolation of wind components carried on the finest mesh (5 km grid spacing) available in the vortex model.

d. Hindcast results

Camille: Certainly some small spatial features in the surface wind field were not modeled; see the comparisons of modeled and measured wind at a site near station 1 (Fig. 16). The wind speed variations observed but not modeled are probably associated with convective spiral rain bands. These perturbations may affect the wave field at least locally, and therefore contribute to wave hindcast errors.

Despite these potential difficulties, we found excellent agreement between modeled and measured sea states at the two measurement sites. Figure 17 compares significant wave height time histories using the grid

TABLE 4. WAM model hurricane validation hindcasts.

Storm	Basin	Date	Measurement site	Type of wave measurement	Source
Hurricane Camille	Gulf of Mexico	August 1969	Station 1 (SP62)	Rig-mounted capacitance wave gauge	Ward (1974)
			Station 2 (WD331)	Rig-mounted capacitance wave gauge	
Hurricane Anita	Gulf of Mexico	September 1977	EB04	Buoy-mounted accelerometer	Forristall et al. (1978)
			EB71	Buoy-mounted accelerometer	
			EI133	Rig-mounted capacitance wave gauge	
Hurricane Frederick	Gulf of Mexico	September 1979	42003	Buoy-mounted accelerometer	Forristall & Reece (1985)
			Cognac	Rig-mounted capacitance wave gauge and electromagnetic current meters	

point closest to the platform locations. The eye of Camille passed about 15 n mi west of station 1 and 50 n mi east of station 2. Valid wave measurements were recorded until the wave staffs were pulled from their underwater connections. This apparently occurred at station 1 just after peak sea states were encountered.

At station 2 wave heights peaked several hours before wave staff failure, though a secondary peak after failure, as suggested in the hindcast, cannot be ruled out.

Figures 18a–c compare estimated and hindcast frequency spectra prior to and at peak conditions at station 1. The inserts display the hindcast two-dimen-
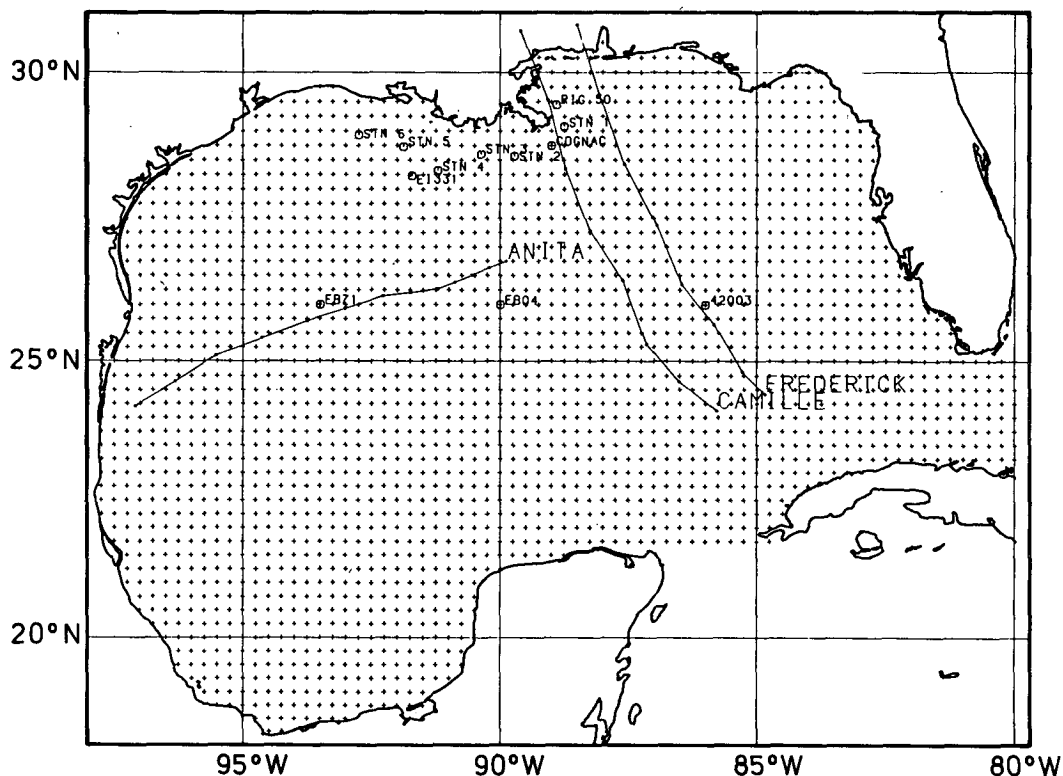
FIG. 15. The WAM model Gulf of Mexico grid system. Hurricane tracks for storm periods modeled and measurement sites are shown.
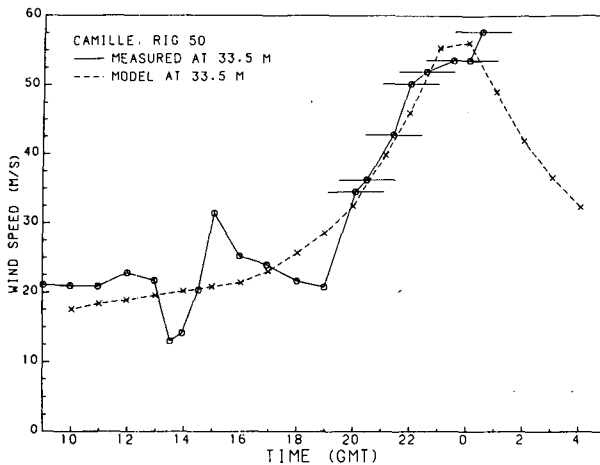
FIG. 16. Comparison of measured and modeled wind speed interpolated from modeled wind field, at RIG 50 (location shown in Fig. 15) anemometer level in Camille. Measured speeds are hourly averages taken from strip chart. Horizontal bars after 2000 UTC estimate timing uncertainty caused by intermittent sticking of chart drive mechanism.

sional spectrum and the local wind (modeled) direction. The agreement between the estimated and hindcast one-dimensional spectra is excellent. At 9 and 3 hours before the eye closed on the station, the spectrum is apparently dominated by swell propagated from the southeast, with only a minor relative high-frequency peak in the two-dimensional spectrum indicated near the local wind direction. The last comparison at 2045 UTC captures the peak sea states in the right front quadrant, where the main part of the energy is now distributed in direction about the local wind direction. It is this low-frequency energy that propagates into the forward quadrant and in the hindcast as swell arriving at station 1 in Figs. 18a–b.

Figure 19 compares the measured spectrum associated with maximum energy at station 2 with the hindcast spectrum at the same time (the hindcast peaked 0.9 m higher 3 hours later). The agreement in spectral shape is good, with the insert again suggesting most of the energy in the main part of the spectrum propagating at right angles to the local wind. Since at this site the local wind is offshore and limited in fetch, there is virtually no local windsea present.

Anita: This hurricane was much less intense than Camille and also moved more slowly. The specification of the wind field in Anita was complicated by the rapid intensification and decrease of the eye diameter during the period modeled, and the irregularities in the shape of the wind field in the formative stage. The effects of wind errors on the wave hindcast are demonstrated in the pattern of differences between measured and modeled significant wave height at the NOAA buoys (Fig. 20), which closely follows the pattern of differences between measured and modeled wind speed (not shown). The wind direction was generally well modeled

at these sites. The third comparison shown in Fig. 20 reveals a good match after the solution is spun up.

Figure 21 compares modeled and measured frequency spectra near peak conditions at the three available sites. The measured spectra are for peak conditions, while the hindcast spectra were selected from the time history at each site such that the difference in total variance between measured and modeled spectra was minimized. The comparisons indicate that the spectral shape and peak frequency of the maximum sea states were modeled correctly.

Frederick: This storm also underwent rapid intensification during the period modeled. The hindcast begins when the storm center is just 80 n mi southeast of the NOAA buoy 42003, and the first 12 hours or so of the run is just model spinup. The early part of the significant wave height time history comparison at the buoy (Fig. 22a) reflects the spinup phase, though the solution appears to capture well the peak sea states recorded at the buoy and the relaxation of seas as the storm moves away. Similarly at Cognac (Fig. 22b), the hindcast sea states are significantly lower than measured during the first 24 hours of the simulation because of insufficient model spinup. After about 1200 UTC 12 September peak sea states are modeled well, but with some lag, which persists through the subsequent decay of the sea state. This lag is not obviously associated with local wind errors.

Figure 23 compares hindcast and measured frequency spectra at the buoy at 0000 UTC 12 September, the time of maximum measured seas. The agreement in spectral shape and the peak frequency is excellent. The general energy level in the hindcast is slightly lower than measured at this time, probably because of the relatively short spinup time available for this site.

Figure 24 compares a series of hindcast and measured frequency spectra and frequency-dependent mean wave direction at Cognac at 2-hourly intervals
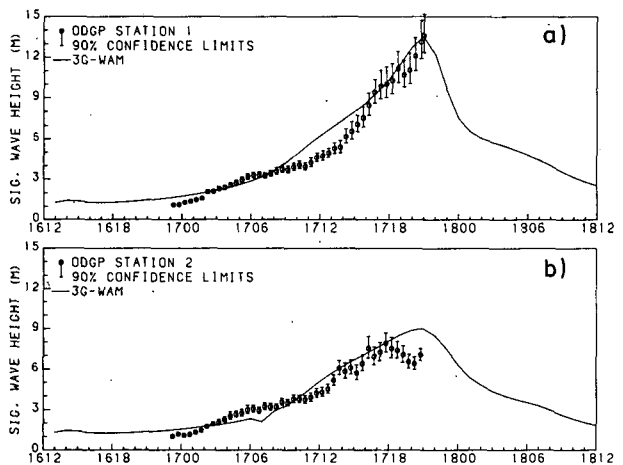

FIG. 17. Comparison of measured and hindcast significant wave height at ODGP deep-water measurement stations 1 and 2 in hurricane Camille.
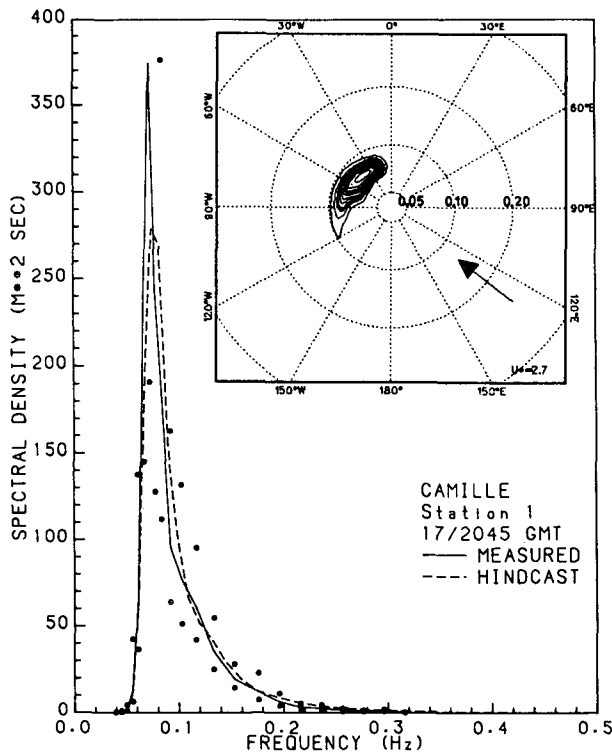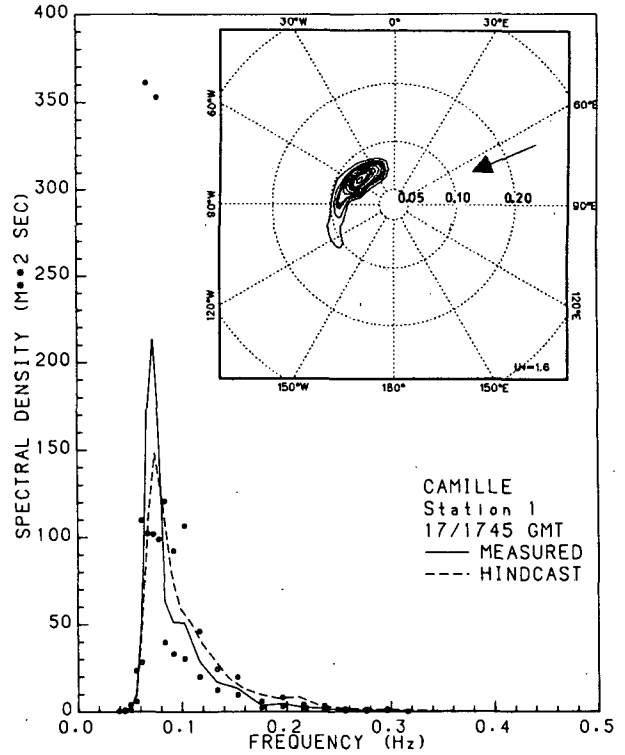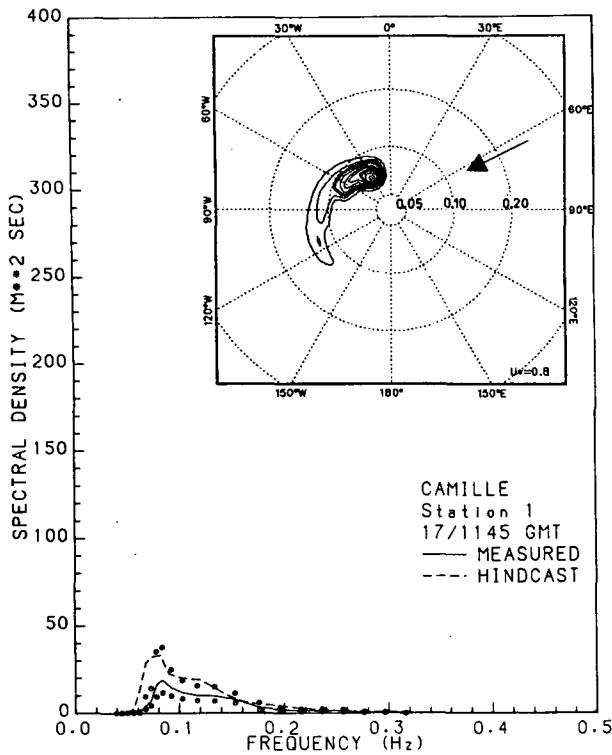
FIG. 18. Comparison of measured and hindcast frequency spectra at station 1 in Camille. (a) 1145 UTC, 9 hours before storm peak; (b) 1745 UTC, 3 hours before peak; (c) 2045 UTC. Confidence limits of individual spectral estimates (90%) also shown. Insert displays corresponding contours normalized to peak value of hindcast two-dimensional spectral density and local wind direction vector.

over a 14-hour period approximately centered on the observed peak sea state. The measured local wind direction at Cognac is also indicated on the wave direction plots.

Leading up to the storm peak, the small underspecification of wave energy in the main part of the spectrum is associated with spectral components whose wave directions propagate north toward Cognac from
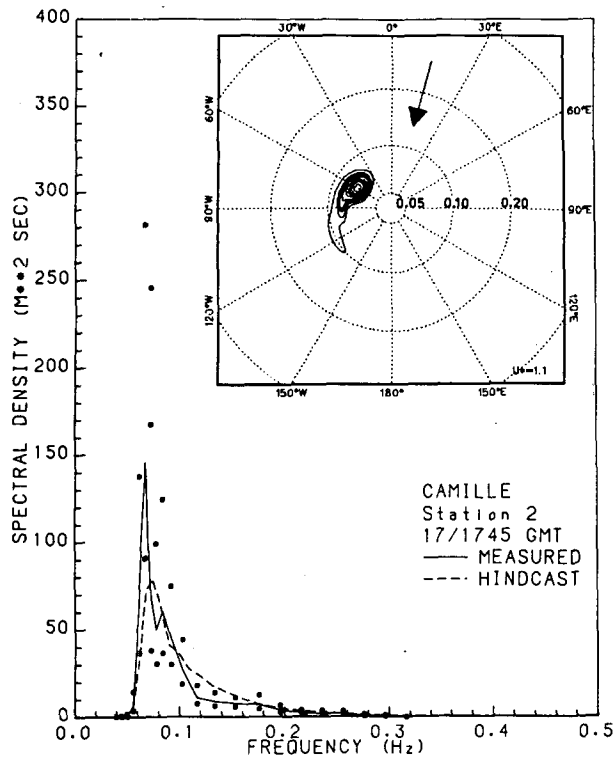
FIG. 19. Measured-hindcast comparisons at time corresponding to peak measured sea state at station 2 in Camille. See Fig. 18 for further explanation.

small bias in the hindcast mean wave direction at 1200 UTC, the mean wave directions in the high-frequency part of the hindcast spectra agree closely with the measurements. This agreement provides encouraging evidence that the directional relaxation of wind seas in a veering wind in the presence of swell is being properly modeled in the WAM model.

In the low-frequency part of the spectrum, the hindcast mean wave direction is about 20° to 30° clockwise from that measured throughout this period. There could be so many factors responsible for this bias (e.g., wind direction errors in the storm's eye wall; directional relaxation effects as the maximum sea states generated near the eye exit the area of maximum winds; propagation effects), that it is difficult to speculate on the source. We should note, however, that the 30-degree bandwidth as used in the present version of the WAM model is a rather coarse directional resolution for simulation of tightly curved wind fields, particularly fields associated with tropical cyclones. It would probably be wise to eventually repeat these hindcasts using an angular resolution of no greater than 15° before seeking an explanation based upon model physics.

Table 5 summarizes the performance of the WAM model in specifying peak sea states at the sites in the general vicinity of the storm center. This underspecification could easily be caused by wind field modeling errors near the center. Our wind model treats a rapidly intensifying hurricane as a sequence of steady states in each of which the wind and pressure fields are assumed to be in equilibrium. Wind field modeling errors near the storm center in effect radiate wave hindcast errors into the far field.

The most interesting parts of the comparisons shown in Fig. 24 are the shape and trend with time of the variation of mean wave direction with frequency over the period shown. The first comparison, at 1100 UTC 12 September, follows a period during which the local wind direction was nearly steady (average direction over the previous 12 hours varied by less than 5° from an average of 237°). The high-frequency components (greater than about 0.15 Hz) are indicated to travel basically downwind at this time. The mean wave direction in and to the left of the spectral peak are about 90° clockwise from the local wind direction. Over the following 8 hours leading up to the storm peak at Cognac, the local wind direction turns at the rate of about 10 degrees per hour, but the high-frequency part of the spectrum lags considerably. For example, by 1900 UTC the tail of the spectrum has evidently turned through only about 30°, while the local wind direction has turned gradually through about 100°. Except for a
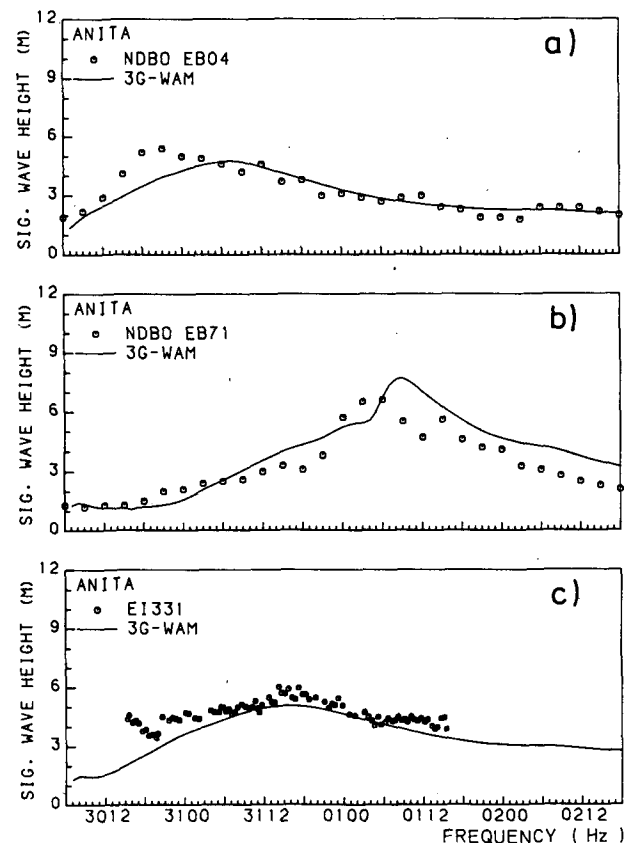

FIG. 20. Comparison of measured and hindcast significant wave height at (a) EB04, (b) EB71, and (c) EI331 in hurricane Anita.

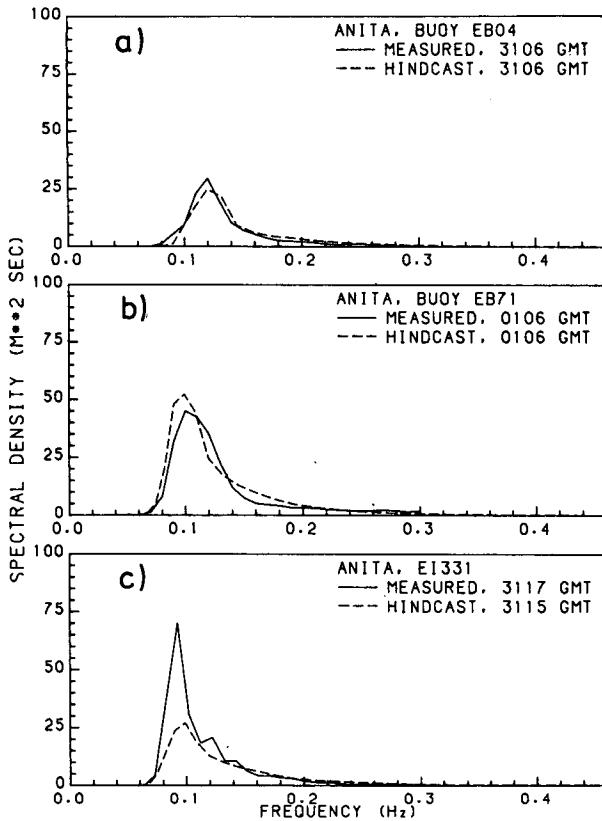FIG. 21. Comparison of measured and hindcast frequency spectra
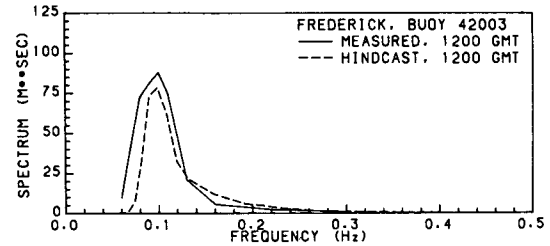at (a) EB04, (b) EB71, and (c) EI331 in hurricane Anita.
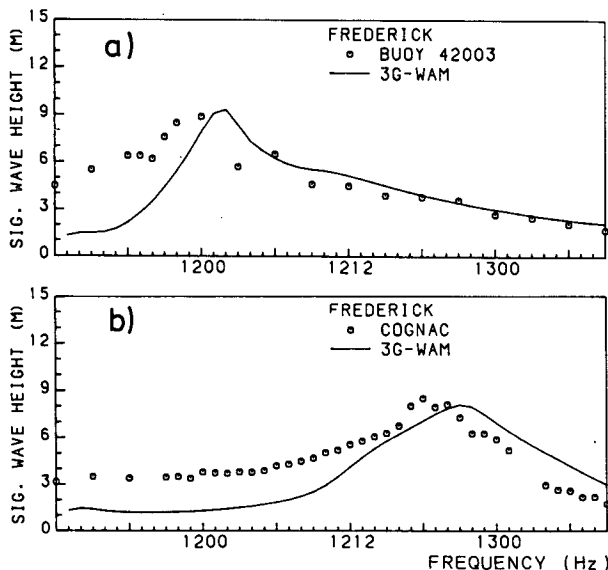
FIG. 23. Comparison of measured and hindcast frequency spectra
(0000 UTC 12 January) at buoy 42033 in hurricane Frederick.

eration models, whose development has usually involved calibration in hurricane wave regimes. However, since the tuning of the WAM model has been confined to pure fetch and duration situations, the encouraging results of the present runs suggests that the WAM model improves upon 1G or 2G models in storm regimes in two ways: first, the new model provides better representation of spectral details, such as the spectral shape and directional spreading; second, the WAM model should provide more reliable results when applied to rarer types of storms (e.g., rapidly propagating intense cyclones) in which measured wave data are not presently available.

8. Global wave hindcast during the SEASAT period

As an example of a global application of the model, a hindcast study was carried out for the entire 96-day SEASAT scatterometer period 7 July–10 October 1978. The input global surface stress fields were constructed by Atlas et al. (1987) from the SEASAT scatterometer data and conventional atmospheric data using a data assimilation system based on the 4° × 5°, nine-level global atmospheric model of the Goddard Laboratory of Atmospheres (GLA).

Alternative surface wind fields have been derived from the SEASAT scatterometer data for the period 6–20 September by Woiceshyn et al. (1987) and the period 6–17 September by Anderson et al. (1987). Woiceshyn et al. used a subjective dealiasing method in combination with a geometric interpolation technique, while Anderson et al. applied the data assimilation system of the European Centre for Medium Range Weather Forecasts, using the ECMWF global T63 model, to combine the dealiased scatterometer data of Woiceshyn et al. with the FGGE dataset. A comparison of the different surface wind/stress products for this period, and an evaluation of the impact of the differences on the hindcast surface wave field, is given in Anderson et al. (1987), Janssen et al. (1987), and Hasselmann et al. (1988). A more detailed comparison of the 96-day global wave hindcast with the SEASAT altimeter wave height and SAR spectral data, and with conventional wave buoy measurements, will be given in a later paper. We present here only a few general features of the global wave hindcast that illus-

three hurricanes studied. The scatter index of 9 percent is comparable to the performance of the more accurate first (e.g., Reece and Cardone 1982) or second generation

FIG. 22. Comparison of measured and hindcast significant wave
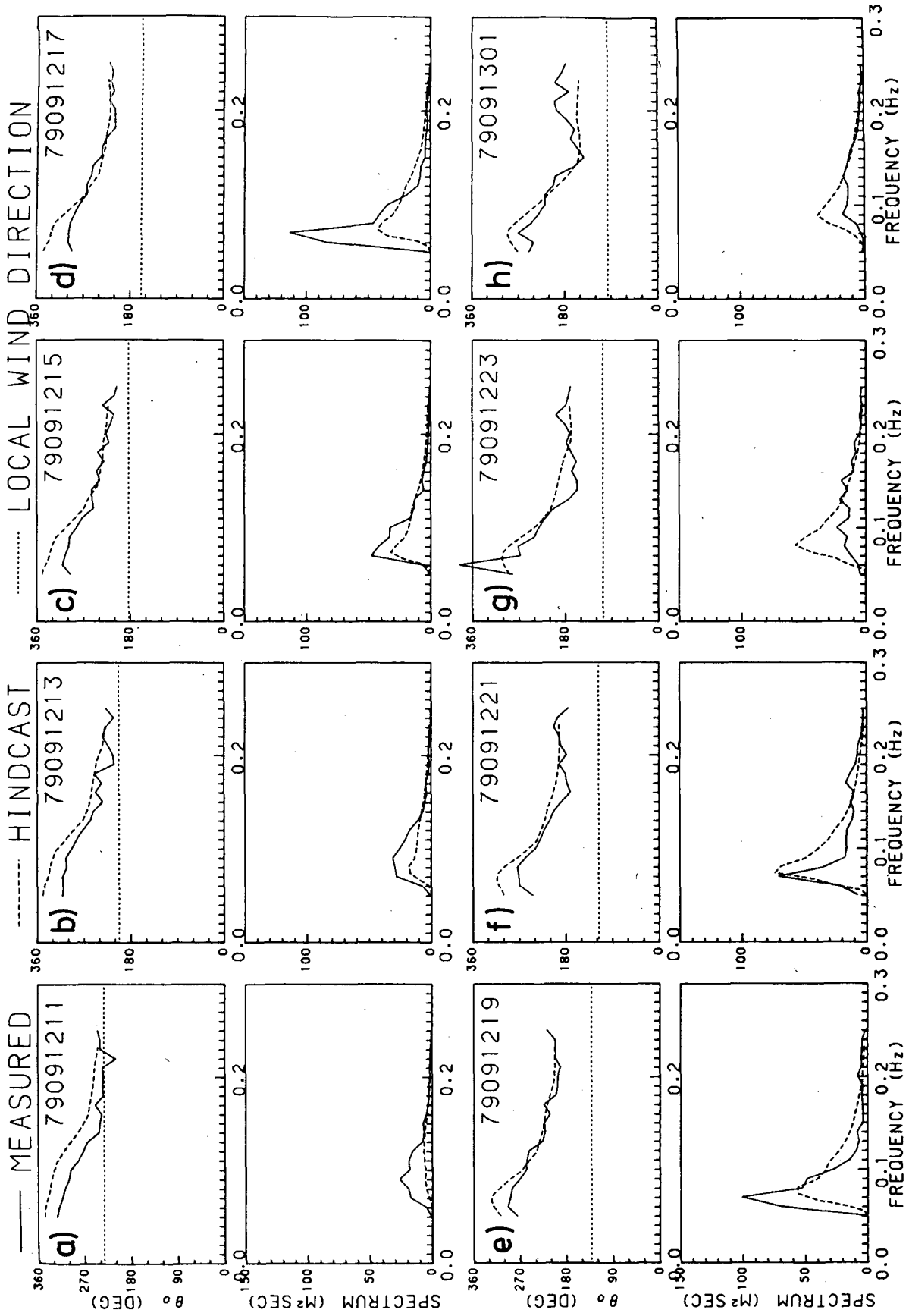height at (a) Cognac and (b) buoy 42003 in hurricane Frederick.

FIG. 24. Comparisons of measured and hindcast frequency spectra and mean wave direction at Cognac at two-hourly intervals in hurricane Frederick. The horizontal dotted line on each plot of wave direction versus frequency is the measured wind direction (to which).

TABLE 5. WAM versus measured peak significant wave height in Gulf of Mexico hurricanes.

Storm	Site	Measured (m)	Hindcast (m)
Camille	ODGPSTN1	13.6	13.5
	ODGPSTN2	7.9	9.0
Anita	EB04	5.4	4.8
	EB71	6.6	7.7
	EI133	6.0	5.1
Frederick	42003	8.9	9.3
	Cognac	8.5	8.1
Mean (m)		8.1	8.2
Root-mean-square (m)			0.70
Scatter index			0.09

trate the type of interconnection between satellite wind and wave data which may be established through global wave models.

Figures 25a, b show a comparison of the average significant wave height for the Southern Hemisphere for the period 1–28 August 1978, computed from the model hindcast and from SEASAT altimeter data by Mognard et al. (1983). The month of August, corresponding to the height of the southern winter, yielded the highest average significant wave heights of the three approximately monthly periods into which the total period 7 July–10 October was subdivided by Mognard et al.

The overall agreement between the computed and observed wave heights is satisfactory at low latitudes, but the high wave energy regions in the "fighting fifties" are clearly underestimated by the model. The comparison of the three surface wind and surface stress fields available for the common two-week period in September suggests that the problem lies in the stress fields. Correlations of the GLA friction velocities with near surface velocity fields, taken either from the GLA analysis itself or from the Anderson et al. (ECMWF) or Woiceshyn et al. (JPL) analyses, yielded consistently lower values for the mean drag coefficient in the high latitude Southern Ocean than in the Northern Hemisphere or the tropics. Since the wave height for a fully developed windsea is directly proportional to the drag coefficient, this discrepancy is sufficient to explain the underestimation of the hindcast wave height field for high southern latitudes.

A cross correlation analysis between the GLA wind field (at 1000 mb) and the ECMWF and JPL wind fields, on the other hand, indicated no systematic biases (less than 10%) between the three wind field analyses (although the differences between individual analyses, particularly in the Southern Hemisphere, were sometimes considerable).

Accordingly, the August hindcast was repeated using the GLA wind field as input instead of the GLA stress. The winds were converted to stresses using the wave

model drag coefficient formulation. This yielded significantly better agreement with the observations (Fig. 25c).

A further indication that the origin of the problem lies in the GLA stress field rather than the wind field analysis may be inferred from the comparison of the three separate wave hindcasts that were carried out for the GLA surface stress field and the JPL and ECMWF wind fields for the September period. Figures 26a–c show the fields of significant wave height for the three hindcasts, averaged over the nine-day period 9–17 September (the first three days of the common period 6–17 September were discarded as spinup). The hindcast for the GLA surface stress field is seen to yield significantly lower wave heights in the Southern Ocean than the other two hindcasts. The ratio of the GLA hindcast wave heights to the ECMWF and JPL hindcast wave heights is of the same order as the ratio of the GLA hindcast wave heights to the altimeter wave heights (Figs. 25a, b), suggesting that the ECMWF and JPL hindcasts are probably realistic and that the hindcast for the GLA stress field is again too low in the high southern latitudes.

We can only speculate here on the cause of these discrepancies. The obvious difficulties of properly capturing intense Southern Ocean storms with a relative coarse resolution model, combined with the almost complete lack of conventional data in the high latitude Southern Ocean, could be part of the explanation. There is also some indication that the SASS scatterometer algorithm underestimates high wind speeds (cf. Anderson et al. 1987). In view of the good performance of the WAM model in the hindcast studies presented above, it appears unlikely that the discrepancies can be attributed to the wave model.

The most probable explanation, however, is that the discrepancies arise from the time averaging involved in the derivation of the surface stress field (Atlas et al., personal communication). In contrast to the wind fields, which are obtained as an essentially instantaneous assimilation product at each synoptic time, the stress fields were computed as six-hourly averages from one synoptic time to the next in the course of the integration of the atmospheric model. The time averaging reduces the rms variability of the stress fields, and since the wave field responds nonlinearly to the stress (the wave energy is approximately proportional to the square of the stress), the mean wave energy is thereby also reduced. The same nonlinearity also explains an underestimate of the drag coefficient inferred from a correlation of the instantaneous wind field with the averaged stress field.

The main point of the above comparisons is to demonstrate that a wave model provides a useful tool for testing the internal consistency of different fields derived from different satellite sensors. The comparison of the wind and wave fields for the September period indicates that the consistency of the data is generally
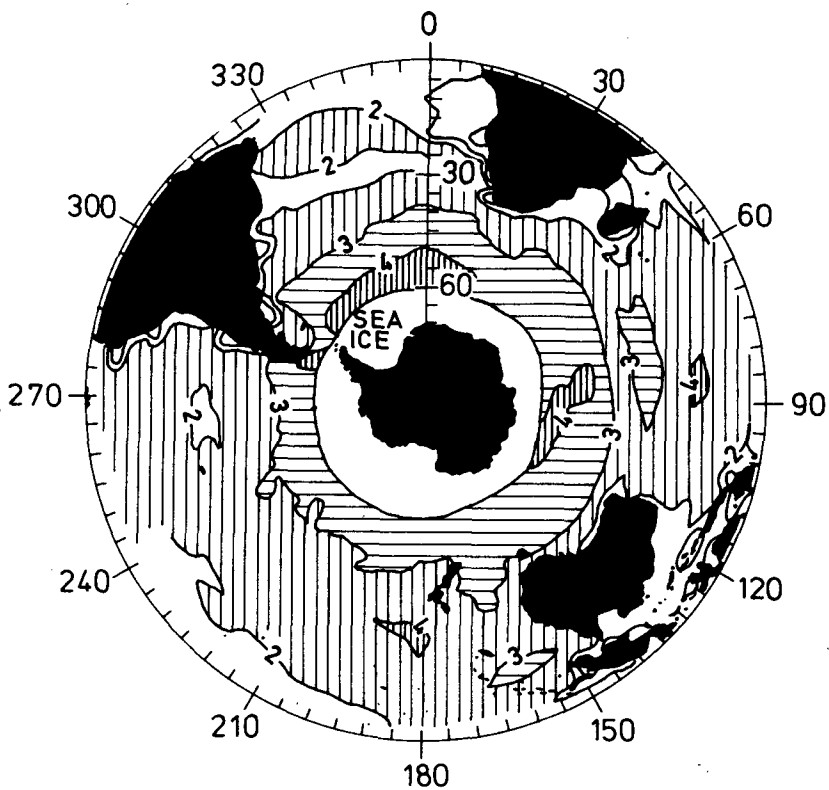
FIG. 25a. Isolines of computed significant wave height for the Southern Hemisphere, averaged over the period 1–28 August 1978 for wave model hindcast using GLA surface wind stress field as input.
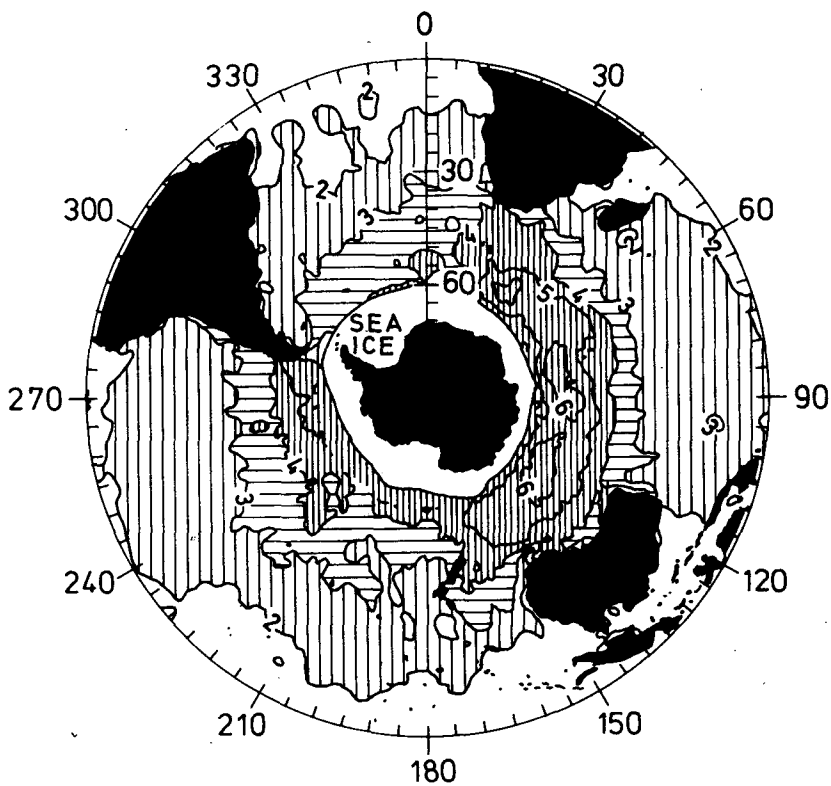
FIG. 25b. Isolines of significant wave height for the Southern Hemisphere, averaged over the period 1–28 August 1978, derived from SEASAT altimeter data (from Mognard et al. 1983).
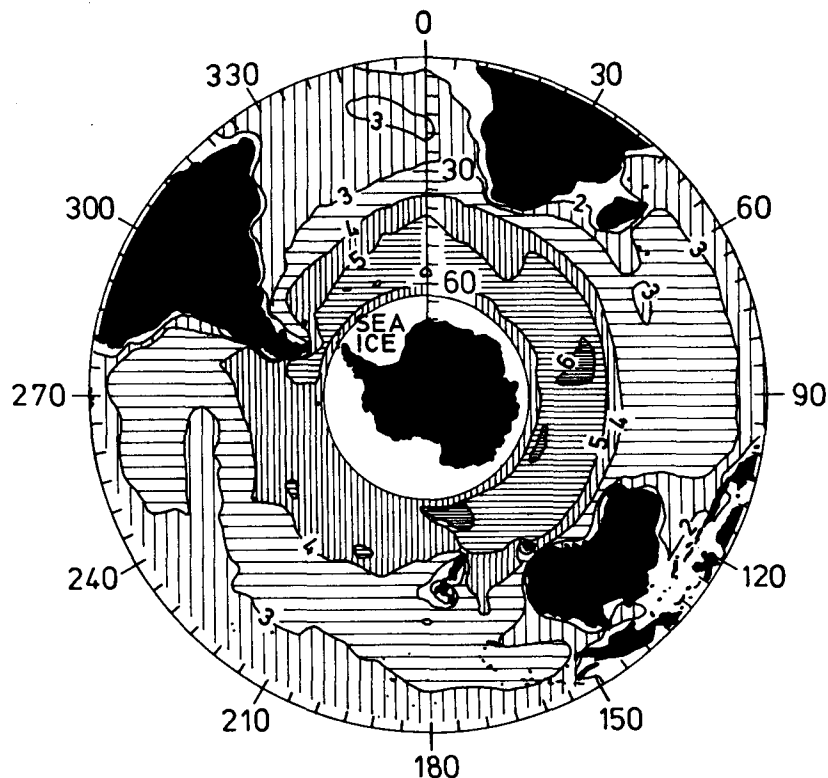
FIG. 25c. As in Fig. 25a, but using GLA surface wind field as input.

much better in the Northern Hemisphere, where more conventional data is available, than in the Southern Hemisphere, which we have emphasized here to illustrate the type of discrepancies that can be revealed by the application of a wave model.

From a comparison of the SEASAT altimeter wave heights within the altimeter wind speeds, Mognard et al. concluded that during the Southern Ocean winter most of the wave energy is associated with swell rather than the local windsea. This finding is supported by the wave model hindcast (including the Southern Ocean itself, the main generation region of the swell).

The separation into windsea and swell, and the reason for the general dominance of the swell field, is seen more clearly in a "snapshot" of the wave field at a particular instant of time. Figures 27–30 show the global surface stress fields and the fields of significant wave height and mean wave propagation direction for the total wave field, windsea, and swell, respectively, on 0000 UTC 19 August 1978. Significant windsea energy is seen to be confined to rather limited regions of strong winds, while the swell energy from the local sources is continually radiated away into the entire ocean. The change in swell propagation direction with increasing distance from the storm centers reflects the movement of the storms, generally from east to west. The windsea was defined in Fig. 29 as that part of the spectrum for which the component of the friction ve-

locity u_* in the direction of wave propagation is greater than $(0.05) \times$ the wave phase velocity (corresponding approximately to $u_* > 1.2c$). The remaining spectrum defines the swell shown in Fig. 30.

Significantly more information on the structure of the wave field is contained in the evolution of the two-dimensional spectra (as illustrated, e.g., in the discussions of the WHIST and hurricane cases in sections 6 and 7). The complete wave spectral information is valuable not only for testing the mutual consistency of the forecast, observed, and analyzed surface wind fields and associated wave fields, but also for initializing the wave field for wave forecasts. Ultimately, the goal of a satellite wind and wave data assimilation system is to jointly initialize both the meteorological fields and the sea state for forecasting and analysis purposes. For a sophisticated assimilation system, high resolution two-dimensional wave spectral measurements are indispensible. In the past, the lack of experimental techniques for obtaining such measurements routinely has presented a serious handicap in wave research. However, SEASAT has demonstrated that spaceborne SARs are able to yield high resolution two-dimensional images of surface waves over large ocean areas, and the planned deployment of SARs in future satellites such as ERS-1 and RADARSAT has given a new impetus to the application of these data in models.

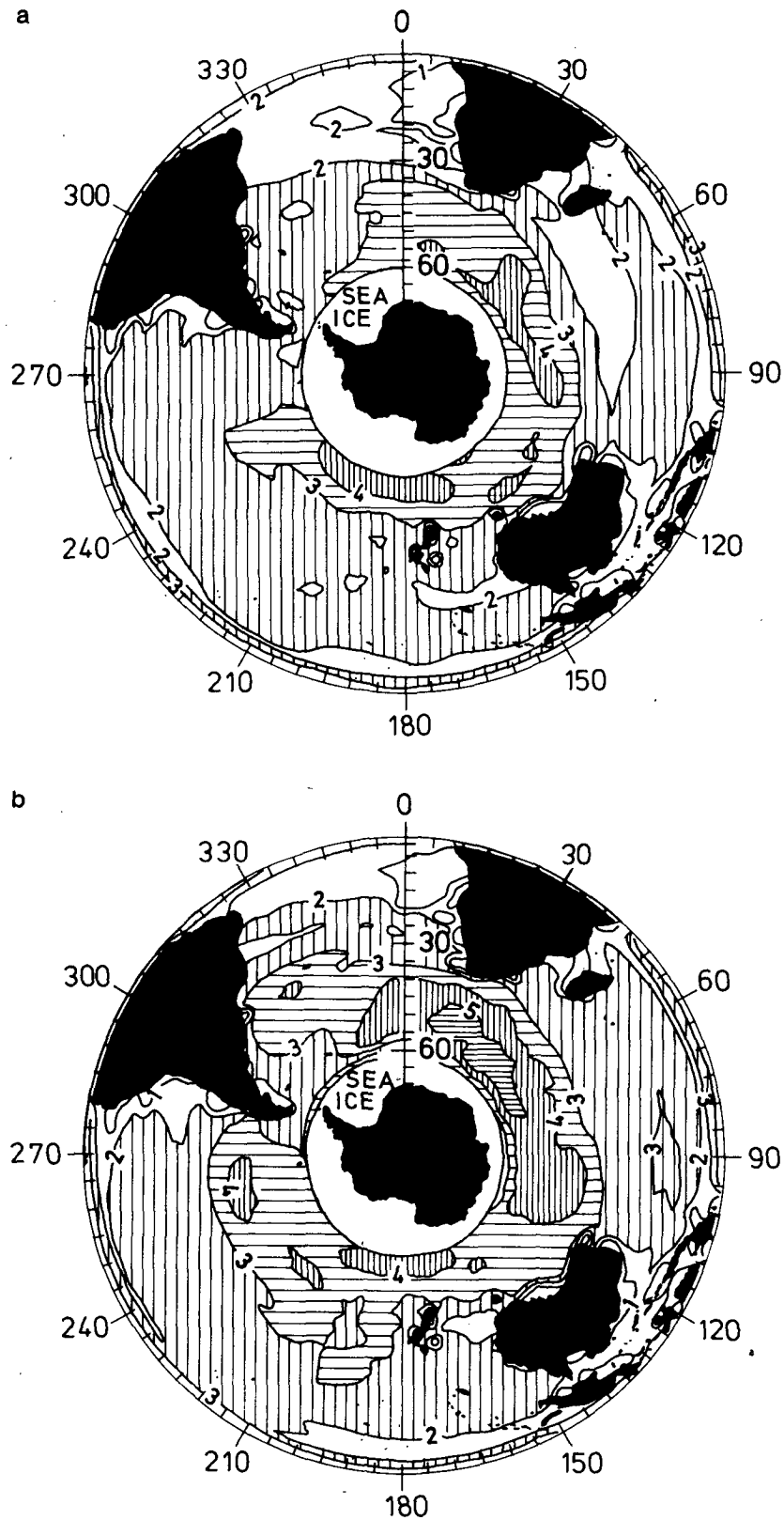However, the interpretation of SAR image spectra

FIG. 26. Isolines of significant wave height for model hindcasts in the Southern Hemisphere, averaged over the period 9–17 September. (a) Surface stress fields from GLA. (b) Surface wind fields from Woiceshyn (1987). (c) Surface wind fields from Anderson et al. (1987).
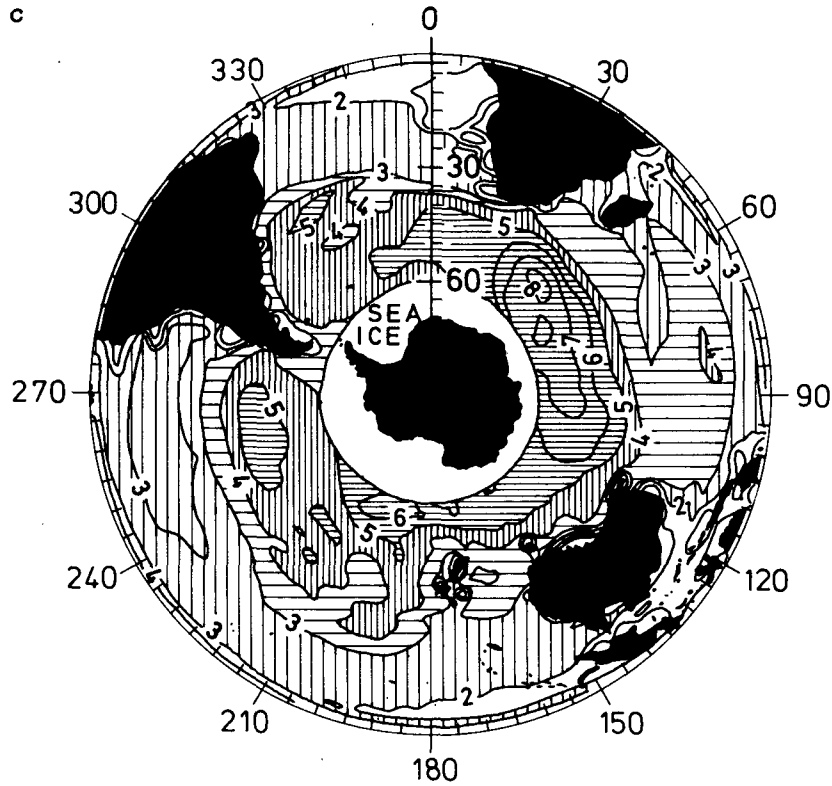
c

FIG. 26. (*Continued*)

in terms of surface wave spectra is not straightforward. Various mechanisms interact in the imaging mechanism (hydrodynamic and tilt modulation, velocity bunching, velocity spreading, and acceleration smearing) (cf. Alpers and Rufenach 1979; Swift and Wilson 1979; Valenzuela 1980; Alpers et al. 1981; Raney 1981;

Hasselmann et al. 1985; and others). For steep windseas of short wavelength, the imaging process can become strongly nonlinear and can lead to a complete smearing out of the wave field in the SAR image spectrum (cf. computations by Brüning et al. 1988). However, over most of the swell-covered ocean, SAR
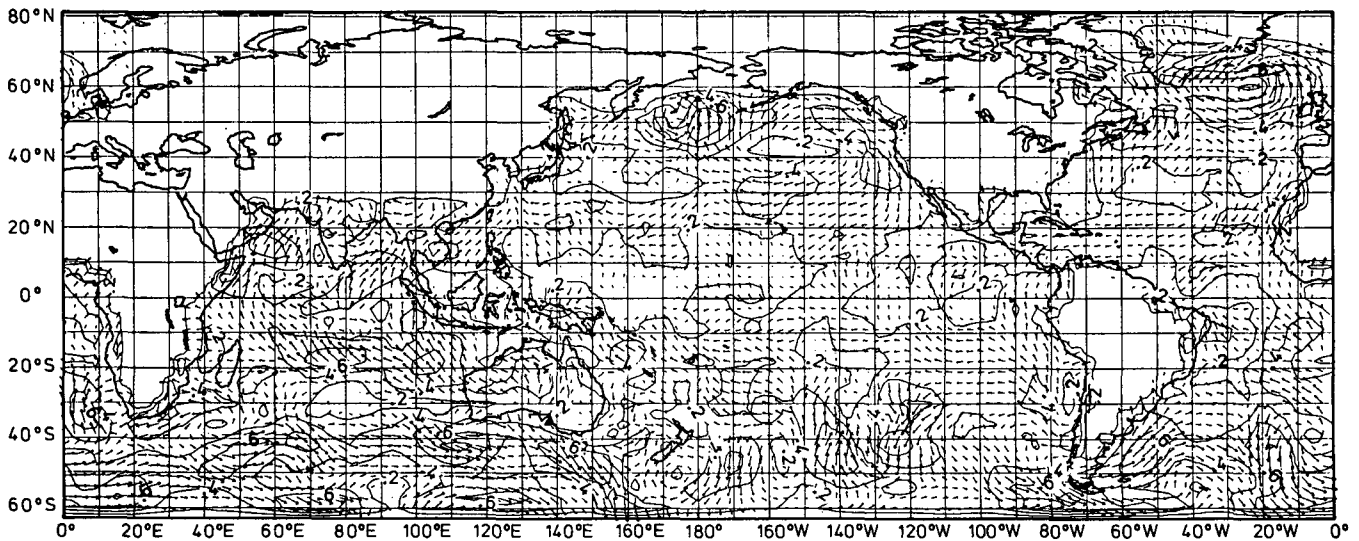

FIG. 27. Global surface stress field, from Atlas et al. (1987), at 0000 UTC 19 August 1987.
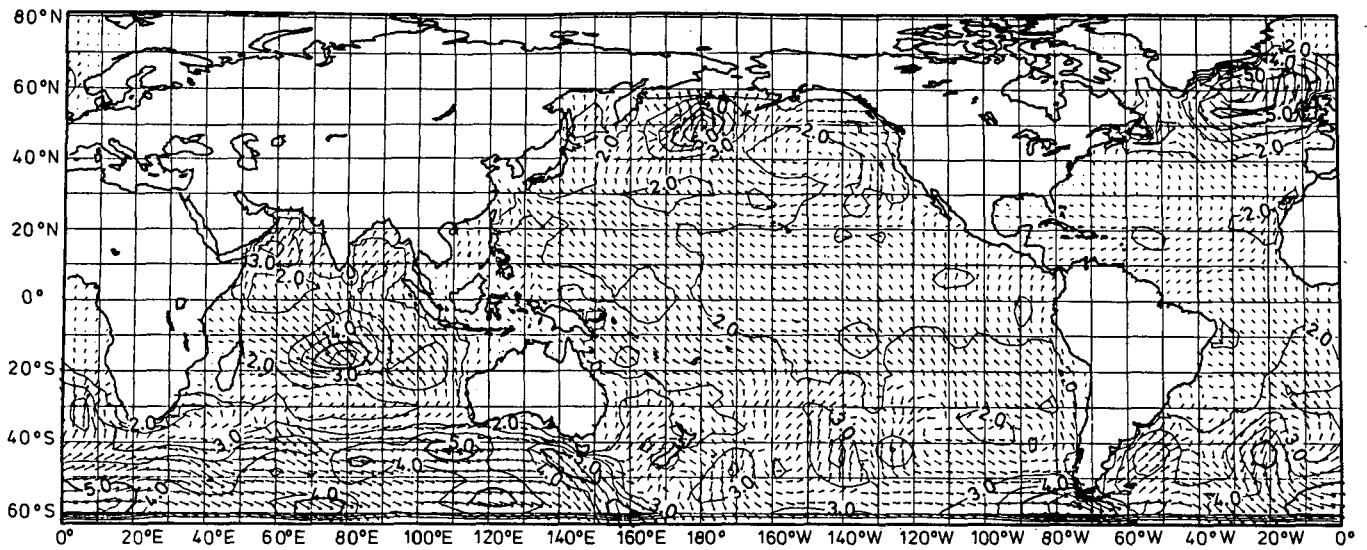
FIG. 28. Significant wave height and mean propagation direction of wave hindcast at 0000 UTC 19 August 1987.
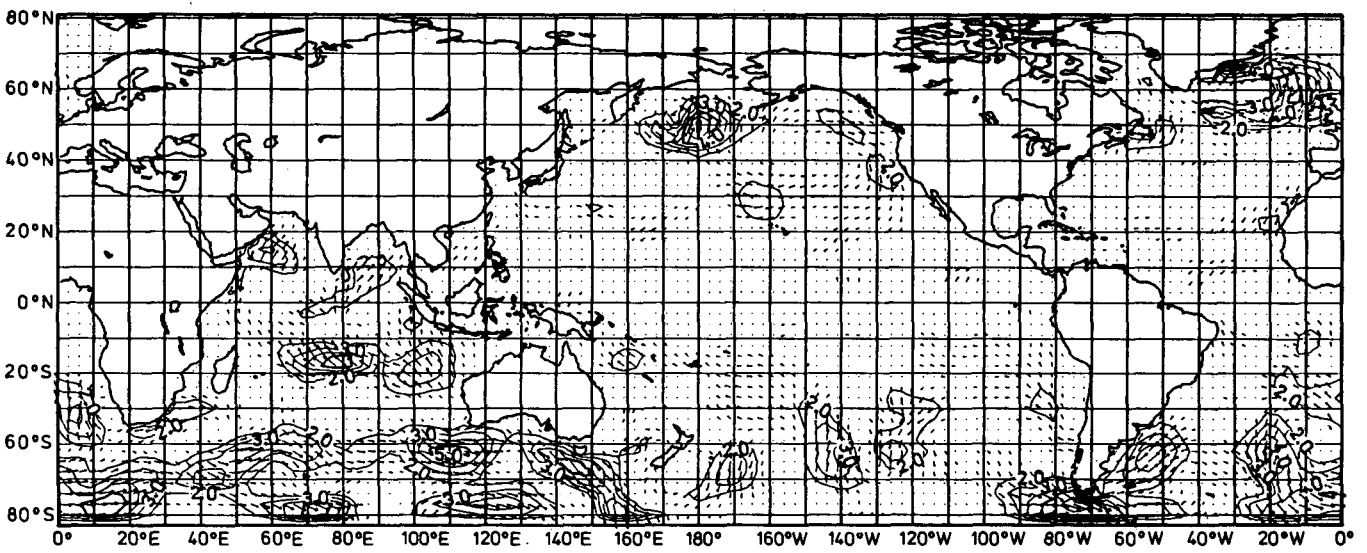

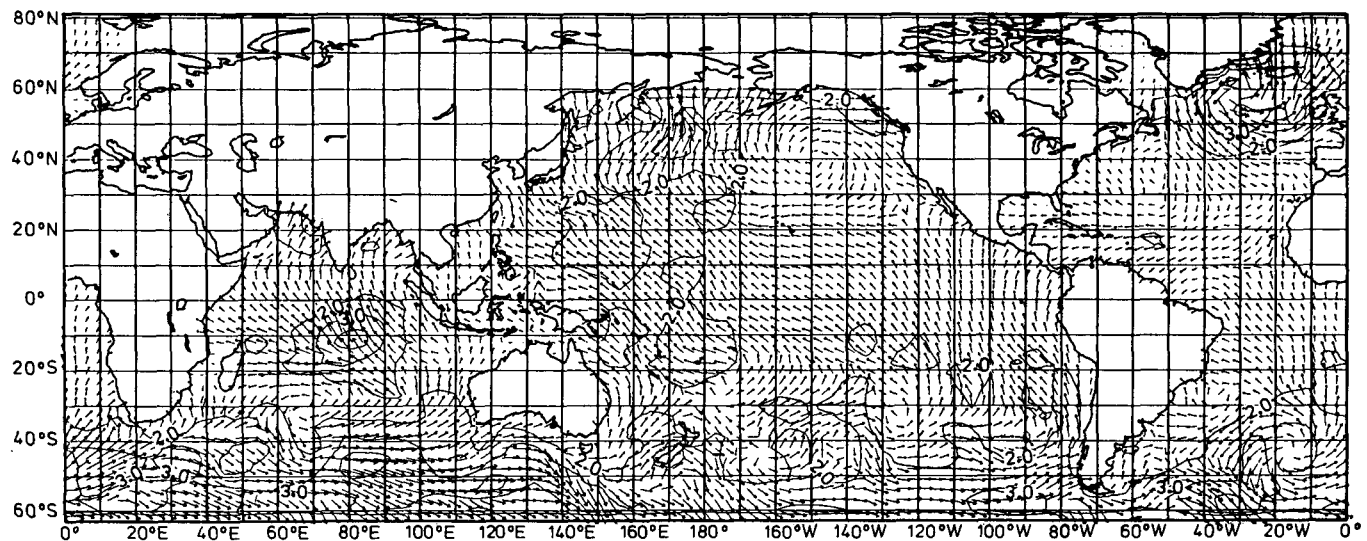FIG. 29. As in Fig. 28 for the windsea component only.

FIG. 30. As in Fig. 28 for the swell component only.

imaging can be regarded as a linear process (albeit, with an inadequately known transfer function).

Some of the promises and problems of SAR wave data are illustrated by the following examples. A more extensive analysis of the SAR image spectra for the North Atlantic, from which these examples were taken, is given in Lehner (1984) and Lehner and Lehner (1988). A detailed comparison of SEASAT SAR spectra with the present wave hindcast is in preparation.

Figure 31 shows a set of swell wave tracks constructed by Lehner (1984) from a sequence of SAR image spectra computed for SEASAT orbit 757 (cf. also Lehner and Lehner 1988 and a similar analysis by Beal et al.

1986). The satellite crossed the North Atlantic on 18 August at approximately 2240 UTC. The swell direction and wavelengths were determined from the wavenumbers of the peaks in the SAR spectra, which were generally rather sharply defined. The swell wavelengths were typically of order 250 m, corresponding to an average propagation time of about 36 hours to the inferred source near 55°N, 38°W.

The GLA surface stress field at 1200 UTC 17 August, corresponding to the estimated time of origin of the swell, and at 0000 UTC 19 August, at approximately the time of the satellite pass, are shown for the region of interest in Fig. 32. The swell and windsea fields at
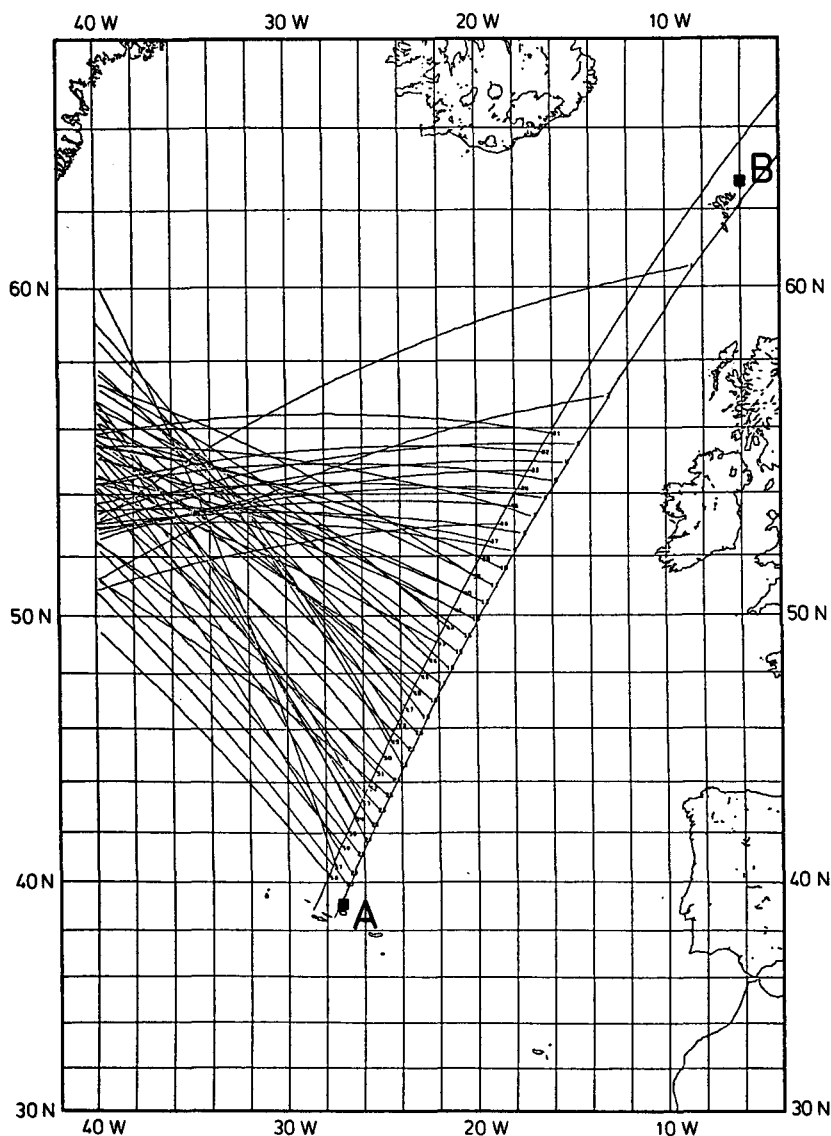

FIG. 31. Wave propagation rays corresponding to spectral peak wavenumber of SEASAT SAR image spectra computed for a sequence of 10 × 10 km sub-images at the near- and far-swath positions indicated for orbit 757 at 2240 UTC on 18 August 1978 (from Lehner 1984). Positions at which the spectra shown in Figs. 34 and 35 were computed are marked A and B, respectively.
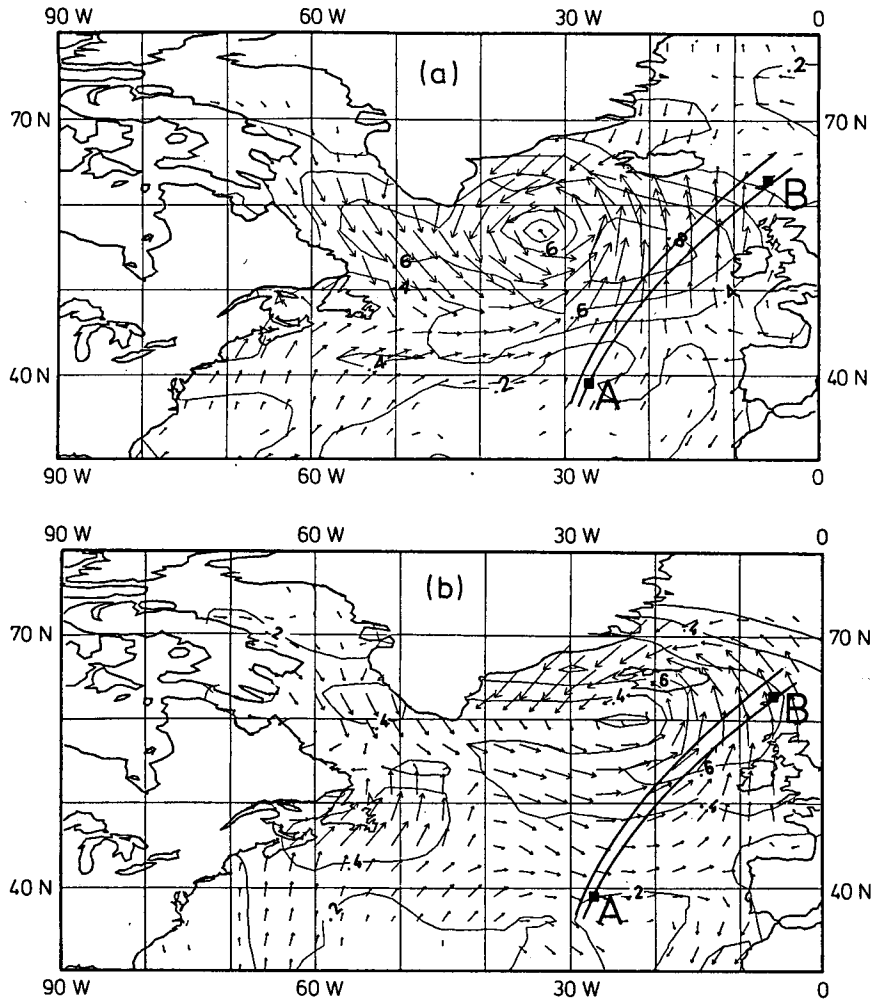
FIG. 32. (a) Surface stress field, from Atlas et al. (1987) at 1200 UTC 17 August 1978, corresponding to estimated time of origin of wave components shown in Fig. 31. (b) Surface stress field at 1800 UTC 19 August 1978, approximately at the time of the SEASAT pass on orbit 757.

the time of the satellite pass, 0000 UTC 19 August, are shown in Fig. 33. The surface stress field at 1200 UTC 17 August (Fig. 32a) should be compared with the swell field at 0000 UTC 19 August (Fig. 33a), while the stress field at 0000 UTC 19 August (Fig. 32b) can be related to the windsea at the same time (Fig. 33b). The general picture inferred from the SAR spectra is clearly consistent with the analyzed surface stress field and wave hindcast.

Detailed comparison of the SAR image spectra for this satellite pass with the two-dimensional wave spectra of the model hindcast generally shows reasonable agreement in the position of the spectral peaks, even when more than one peak is present. Examples are given in Figs. 34 and 35.

To relate the SAR image spectrum to the wave spectrum, the original image wavenumber spectrum $F_I(\mathbf{k})$ was converted in Figs. 34 and 35 to an equivalent polar $f - \theta$ wave height spectrum $F_I(f, \theta)$, using the surface

wave dispersion relation and an isotropic transfer function $\sim k$, (which has occasionally been proposed as a first approximation):

$$F_I(f, \theta) \sim F_I(k)\left(\frac{dk_1 \, dk_2}{df d\theta}\right)\frac{1}{k} \sim F_I(k)f. \quad (8.1)$$

The quantitative interpretation of the SAR image spectral levels is still an open question. Compared with the wave spectrum of Fig. 35b, for example, the peak in the SAR spectrum of Fig. 35a, representing a swell train propagating in the northerly direction, appears strongly enhanced relative to the shorter wavelength peak representing a windsea propagating in the northwesterly direction (for interpretation of the peaks, cf. Figs. 32–33). Figure 35 indicates that the transfer function is not as simple as assumed in (8.1) (as is indeed to be expected theoretically; for the relatively low wave slopes of the spectra shown in Figs. 34 and
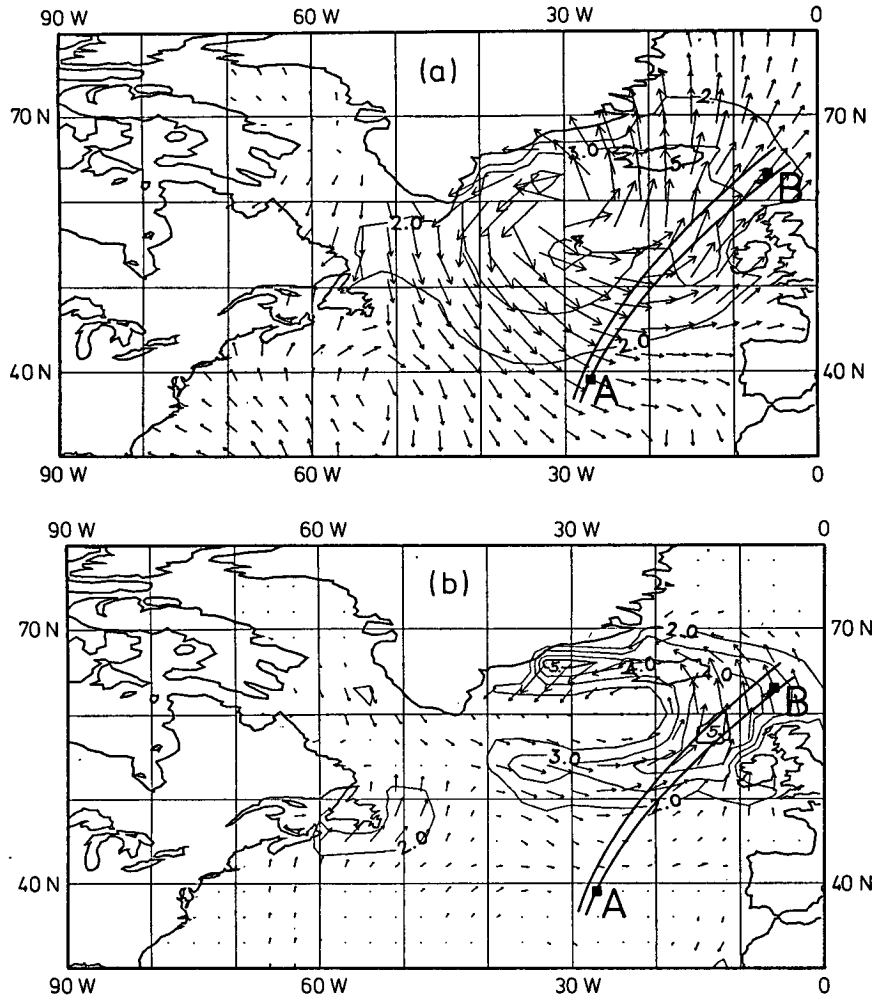
FIG. 33. Hindcast wave field at 1800 UTC on 19 August 1978, approximately at the time of the SEASAT pass. (a) Swell height and propagation direction. (b) Windsea wave height and propagational direction.

35, however, it can probably at least be assumed that the imaging mechanism is linear and can therefore be characterized by a transfer function).

An example of a SAR image spectrum that is clearly already contaminated by nonlinear effects is given in Fig. 36. The SAR image was obtained in this case from SEASAT orbit 1359 at 0117 UTC 30 September at a position north of Scotland fairly close to a severe storm in the North Sea to the southeast (cf. Lehner 1984; Lehner and Lehner 1988). The SAR spectrum exhibits a pronounced azimuthal high wavenumber cutoff, i.e., an attenuation of short waves propagating parallel to the satellite flight direction. The SAR spectrum shows little similarity with the computed wave spectrum. The windsea peak in the northwest quadrant is reproduced in approximately the right direction, but the SAR wavelength is too long, and the azimuthally traveling swell in the northeast quadrant is barely detectable. Qualitatively similar features have been reproduced in

the Monte Carlo simulations of Brüning et al. (1988) in the nonlinear imaging regime.

In summary, it appears that SAR image spectra can exhibit promising high-resolution details, which in the linear regime correspond rather closely to the structure of the two-dimensional model wave spectra, but an application of this data for quantitative model verification or data assimilation purposes requires further clarification of the linear and nonlinear transformation properties relating SAR image and ocean wave spectra.

9. Conclusions and outlook

The third generation model presented in this paper integrates the basic spectral transport equation without any side conditions on the form of the evolving spectrum. Tuning was carried out only for infinite depth, fetch-limited growth to determine two free parameters in the dissipation source function. The response of the
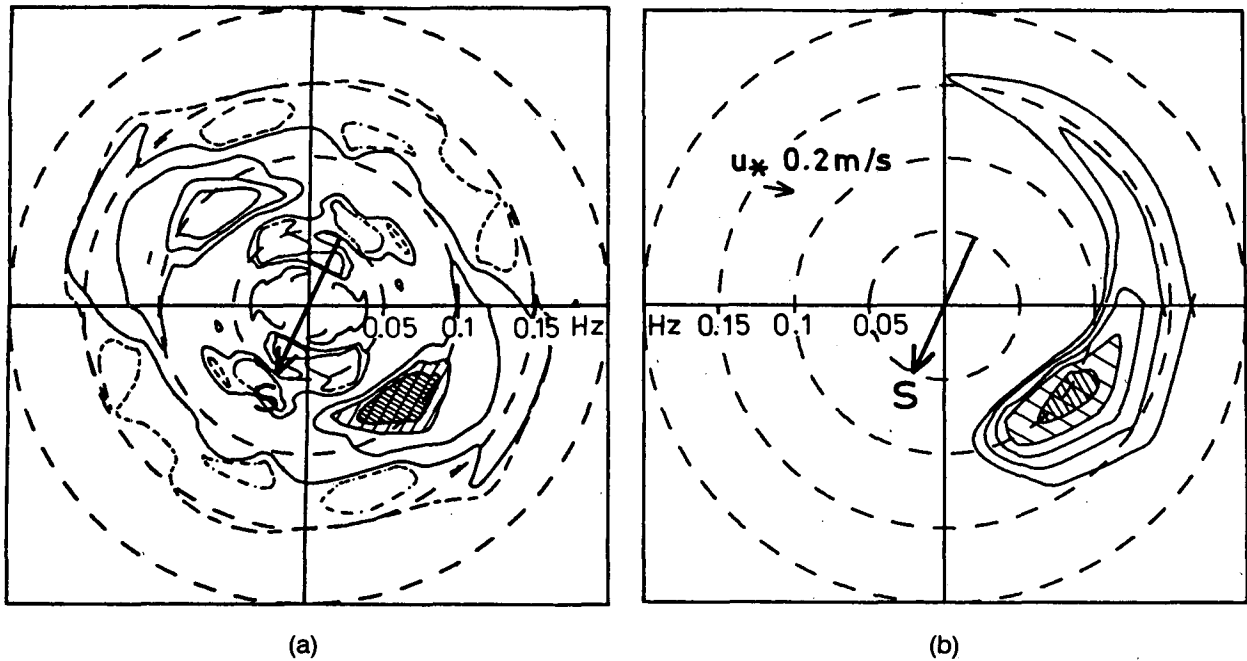
FIG. 34. (a) SAR image spectra, from Lehner (1984) and (b) hindcast model wave spectrum at station A along the SAR swath (for interpretation of Figs. 31–33). The SAR wavenumber spectrum has been converted to an equivalent frequency direction spectrum in accordance with Eq. (8.1). The SAR flight direction is denoted by S. The spectrum contains only one swell peak.

model for arbitrary wind fields is then determined solely by the structure of the three basic source functions S_{in}, S_{nl}, and S_{ds} and the finite depth bottom friction source function S_{bf}.

The model was tested for six North Atlantic–North Sea storms and three Gulf of Mexico hurricanes. The overall agreement with observations for these regional hindcasts was good. A global 96-day integration was
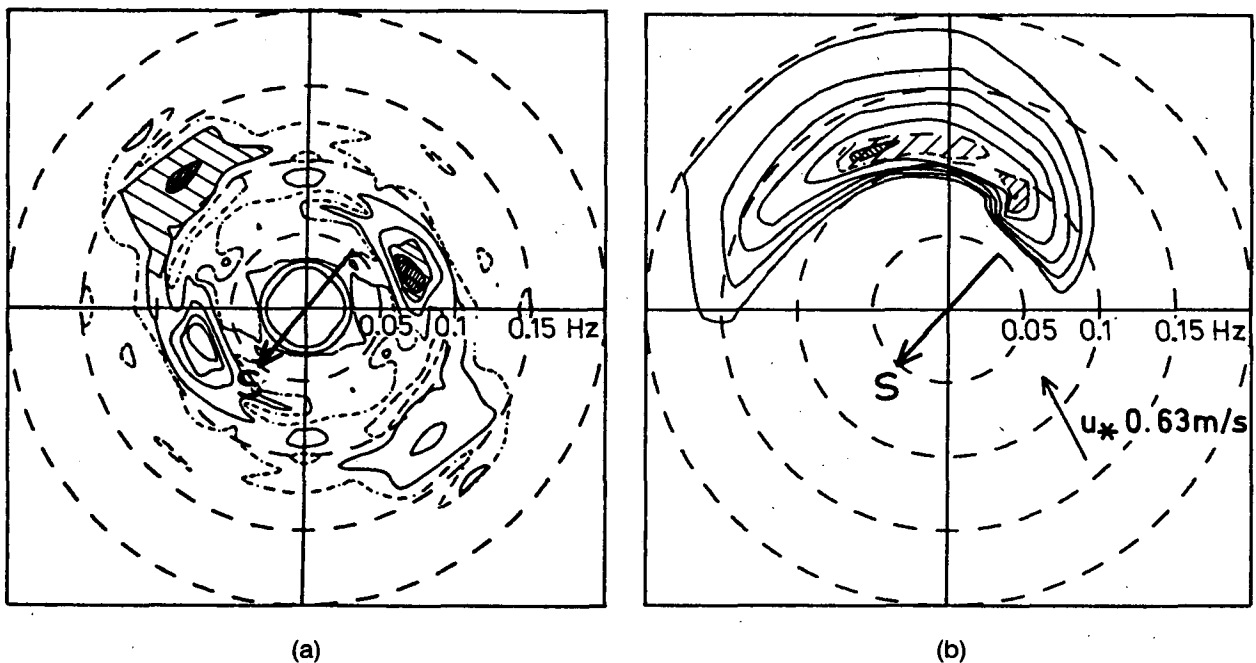

FIG. 35. As in Fig. 34 at station B. The spectra contains both a swell peak and a windsea peak, (for interpretation, cf. Fig. 32b) the local wind direction is indicated by W.
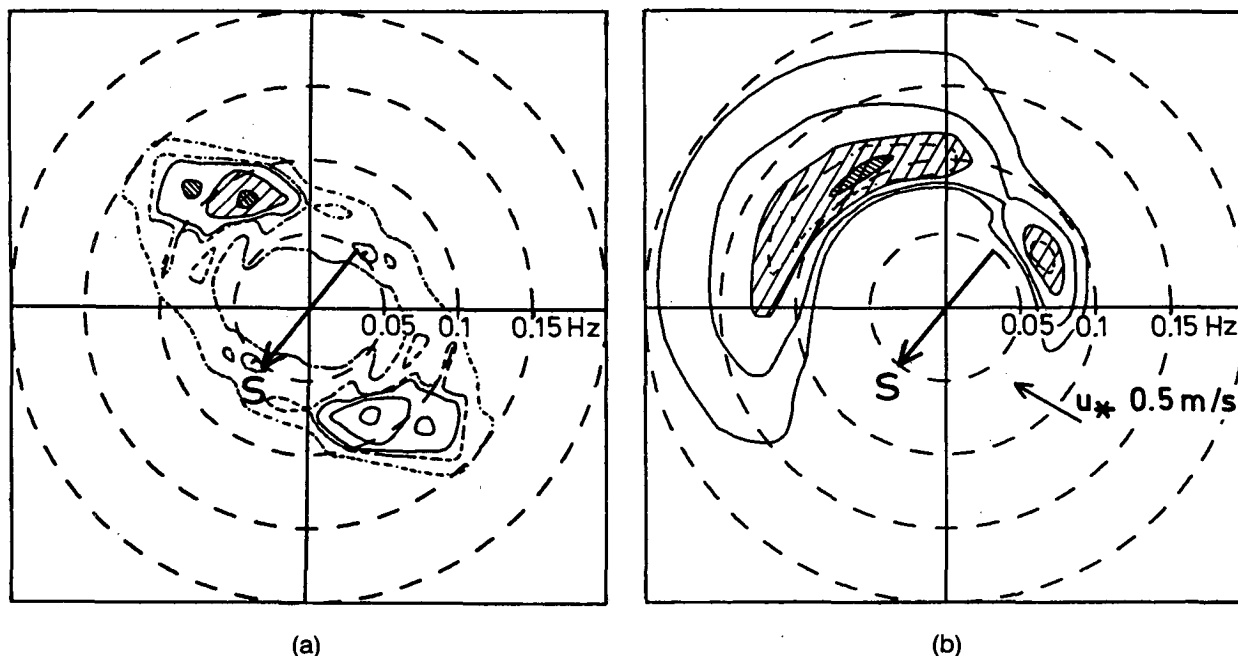
(a) (b)

FIG. 36. As in Fig. 34 for a position north of Scotland close to a North Sea storm to the southeast. Note the pronounced azimuthal high wavenumber cutoff for waves propagating orthogonal to the SAR-look direction (i.e., satellite flight direction) and the shift of the peak wavenumber to lower values in the SAR spectrum.

also carried out, using as input the surface stress fields constructed by Atlas et al. (1986) from the SEASAT scatterometer data and conventional atmospheric data using a model data assimilation method. The results of the global hindcast were generally consistent with the wave height fields derived from the SEASAT altimeter by Mognard et al. (1983) and the SEASAT SAR spectra analyzed by Lehner (1984). However, the altimeter wave heights were significantly underestimated by the model hindcast in the high wind belt around 50°S, probably indicating deficiencies in the analyzed stress fields in this region.

Although the hindcast tests presented here are encouraging, further tests of the input and dissipation source functions, in particular for high wind and sea states, would be desirable. Another process that would be useful to test more carefully is the radiation of swell out of a windsea source region, since this is a unique feature that only a third generation model can reproduce without additional tuning.

An important motivation for the development of a third generation wave model was to provide a properly formulated global wave model, based on physical first principles, in time for the launch of the next generation ocean satellites in the early 1990s. Improved wave models will be needed at this time to properly exploit the greatly expanded surface wind and wave data base provided by these satellites for wave forecasting and other applications. In addition, wave models will then be required for extended data assimilation schemes in

conjunction with atmospheric models. It is a characteristic feature of most microwave sensors flown on ocean satellites that the signals contain mixed signatures depending on both the surface wind and the sea state. To incorporate these interactions in improved sensor algorithms, data assimilation systems are needed in which the surface wind and wave data are analyzed simultaneously. A combined analysis and assimilation system is required not only for real time forecasting application but also to produce continuous, global, gridded datasets for oceanographic and climate research. Such systems can presumably be implemented only at operational forecasting centers through the joint efforts of operational and research groups.

Wave data assimilation is a relatively new problem for wave modelers. The combined assimilation of both surface wave data and meteorological data is a new field for both meteorologists and wave modelers. Considerable efforts will therefore be needed to establish an operational, comprehensive atmospheric and surface wave data assimilation system to make optimal use of the data of future oceanographic satellites. The present work may be viewed as a contribution toward this goal.

APPENDIX A

Great Circle Propagation Relations

The great circle path of a wave group on the spherical earth may be written in the form

$$\mathbf{x} = R\left[\mathbf{e}_c \cos\frac{vt}{R} + \mathbf{e}_s \sin\frac{vt}{R}\right] \qquad (A1)$$

where R is the radius of the earth, v the group velocity,

$$\mathbf{e}_c = \begin{cases} \cos\phi_0 \cos\lambda_0 \\ \cos\phi_0 \sin\lambda_0 \\ \sin\phi_0 \end{cases} \qquad (A2)$$

$$\mathbf{e}_s = \begin{cases} -\cos\theta_0 \sin\phi_0 \cos\lambda_0 + \sin\theta_0 \sin\lambda_0 \\ -\cos\theta_0 \sin\phi_0 \sin\lambda_0 - \sin\theta_0 \cos\lambda_0 \\ \cos\theta_0 \cos\phi_0 \end{cases} \qquad (A3)$$

are orthogonal unit vectors pointing in the direction of the location and velocity, respectively, of the wave group at time $t = 0$; $\phi_0, \lambda_0, \theta_0$ denote the initial spherical coordinates and propagation direction of the wave group at time $t = 0$. The vector $\mathbf{e}_s$ can be readily recognized as the wave group propagation direction by considering first the special case $\theta_0 = 0$, $\lambda_0 = 0$ and then rotating about the r-axis ($\theta_0 \neq 0$) and subsequently about the z-axis ($\lambda_0 \neq 0$) to recover the general case.

Differentiating (A1) with respect to t and setting $t = 0$ yields the propagation equations (2.2) and (2.3). To derive the refraction equation (2.4) we note that

$$\cos\theta = \frac{1}{v}\left(\frac{d\mathbf{x}}{dt} \cdot \mathbf{e}_n\right) \qquad (A4)$$

where

$$\mathbf{e}_n = \begin{cases} -\sin\phi \cos\lambda \\ -\sin\phi \sin\lambda \\ \cos\phi \end{cases} \qquad (A5)$$

is the local northward-pointing horizontal unit vector. Differentiating (A4) we obtain

$$\frac{d\theta}{dt}\sin\theta = \frac{1}{v}\left\{\frac{d^2\mathbf{x}}{dt^2} \cdot \mathbf{e}_n + \frac{d\mathbf{x}}{dt} \cdot \frac{d\mathbf{e}_n}{dt}\right\} = \frac{1}{v}\frac{d\mathbf{x}}{dt} \cdot \frac{d\mathbf{e}_n}{dt}, \qquad (A6)$$

which yields (2.4) on substitution of (A1) and (2.2), (2.3) into $d\mathbf{x}/dt$ and $d\mathbf{e}_n/dt$. A more detailed discussion of wave propagation on a sphere is given in Groves and Melcer (1961).

APPENDIX B

Second-Order Propagation Scheme

In the leapfrog advection scheme (4.10), even grid points at even time levels $n, n + 2, n + 4, \ldots$ (n even) are coupled with odd grid points at odd time levels $n + 1, n + 3, n + 5, \ldots$. This "even" space–time grid does not interact with the complementary staggered "odd" space–time grid composed of odd spatial grid points at even time levels and even spatial points at odd time levels ("spatial" applies here to the three dimensions ϕ, λ, and θ). In the second-order scheme used in the present model, the wave field was accordingly defined only on the even grid. However, a straightforward centered difference discretization of the diffusion operator indicated in (4.10) introduces odd space–time grid points. Some form of interpolation is therefore needed to express these in terms of even grid points. Various methods can be used.

A relatively simple energy-conserving scheme is to apply advection and diffusion operators alternatively, the diffusion operators smoothing the fields at a given time level. (In terms of the time integral, they may be interpreted as acting over intermediate time intervals centered at $n + \frac{1}{2}, n + \frac{3}{2}, n + \frac{5}{2}, \ldots$.) To maintain basically the same data structure for both first- and second-order versions of the model, the fields at even grid points at the time level n were combined with the fields at odd grid points at time level $n + 1$ into a single composite field assigned to a single time level. The integration was then stepped forward in double steps to $(n + 2, n + 4)$, etc. The diffusion operator was represented as a superposition of forward and backward diffusion operators $D_\wedge$ and $D_\vee$ which could be combined into a composite operator $D_c = D_\wedge + D_\vee$ acting on the composite field. A double integration step consists then of a sequence of four operations D_c, A, D_c, A (A = advection) involving the generation of two intermediate spectra F', F''. The cycle is identical, except for a shift, for even and odd time levels and even and odd spatial grid points.

Assuming the cycle begins with the given spectra F^n, F^{n+1}, the sequence of operations is specified as (see also Fig. B1)

$$(F^n, \bar{F}^{n+1}) = D_c(\bar{F}^n, F^{n+1})$$
$$= D_\wedge(\bar{F}^n, F^{n+1}, \bar{F}^n) + D_\vee(F^{n+1}, \bar{F}^{n+1}) \quad (B1)$$
(all composite grid points)

$$F^{n+2} = A(F^n, \bar{F}^{n+1}), \quad \text{even grid points only} \quad (B2)$$

$$(F^{n+1}, \bar{F}^{n+2}) = D_c(\bar{F}^{n+1}, F^{n+2})$$
$$= D_\wedge(\bar{F}^{n+1}, F^{n+2}, \bar{F}^{n+1})$$
$$+ D_\vee(F^{n+2}, \bar{F}^{n+1}, F^{n+2}),$$
(all composite grid points) $\quad (B3)$

$$F^{n+3} = A(F^{n+1}, \bar{F}^{n+2}), \quad \text{(odd grid points only)} \quad (B4)$$

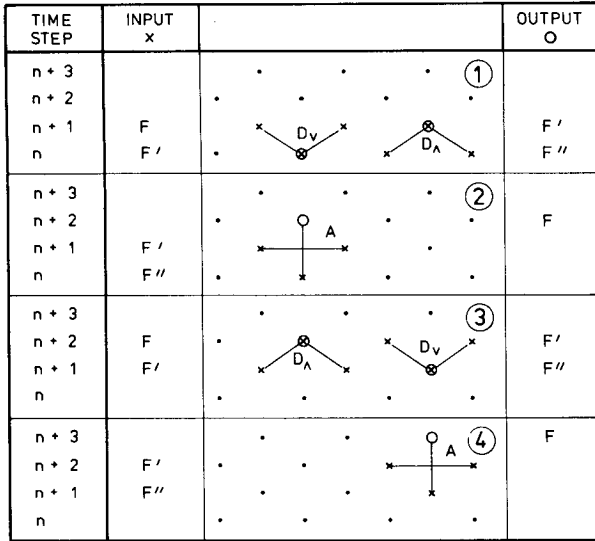| TIME STEP	INPUT x		OUTPUT O
n + 3		· · · ①	
n + 2		· · · ·	
n + 1	F	×＼D_v／× ／⊗$D_\wedge$＼×	F ′
n	F ′	· ＼⊗／ ×＼ ×	F ″
n + 3		· · · ②	
n + 2		· ○ A · ·	F
n + 1	F ′	×—+—× ·	
n	F ″	· · · ·	
n + 3		· · · ③	
n + 2	F	· ／⊗＼ ×＼D_v／×	F ′
n + 1	F ′	×$D_\wedge$＼× ＼⊗／	F ″
n		· · · · ·	
n + 3		· · ○ A ④	F
n + 2	F ′	· · ×—+—×	
n + 1	F ″	· · · +	
n		· · · ·	

FIG. B1. Second-order leapfrog advection and diffusion scheme. Diffusion is applied at all grid points alternatively as forward and backward operators D_v, $D_\wedge$ between advection steps, which are applied alternatively at even and odd grid points. Diffusion smoothing is applied formally at a fixed time level. The four-step sequence shown advances the field from the time levels n, $n + 1$, to $n + 2$, $n + 3$. Input grid points: x; output grid points: O.

where the operators are defined (in the notation of section 4b) as

$$\bar{F}_j^{n+1} = D_\wedge(\bar{F}^n, F^{n+1}, \bar{F}^n)$$

$$= F_j^{n+1} + \sum_k \frac{\Delta t D_k}{2(\Delta x_k)^2 \cos\phi_j} [(\bar{F}^n \cos\phi)_{k_+}$$

$$+ (\bar{F}^n \cos\phi)_{k_-} - 2(F_j^{n+1} \cos\phi_j)] \quad (B5)$$

$$F_j^n = D_v(F^{n+1}, \bar{F}^n, F^{n+1})$$

$$\equiv \bar{F}_j^n + \sum_k \frac{\Delta t D_k}{2(\Delta x_k)^2 \cos\phi_j} [(F^{n+1} \cos\phi)_{k_+}$$

$$+ (F^{n+1} \cos\phi)_{k_-} - 2(\bar{F}_j^n \cos\phi_j)] \quad (B6)$$

$$F_j^{n+2} = A(\bar{F}^n, F^{n+1}) = \bar{F}_j^n - \sum \frac{\Delta t}{2\Delta x_k \cos\phi_j}$$

$$\times [(v \cos\phi \bar{F}^n)_{k_+} - (v \cos\phi \bar{F}^n)_{k_-}] \quad (B7)$$

In the second-order propagation example shown in Fig. 2, the angular diffusion coefficient $D_k^{(\theta)}$ was set equal to zero, while the latitude and longitude diffusion coefficients were chosen respectively as

$$\{D_k^\phi, D_k^\lambda\} = 2.6 \times 10^{-7} \Delta t f^{-1} g \{\Delta\phi, \Delta\lambda\} \ \sec^{-1}.$$

REFERENCES

Alpers, W., and C. L. Rufenach, 1979: The effect of orbital motions on synthetic aperture radar imagery of ocean waves. *IEEE Trans. Antennas Propag.*, AP 27, 685–690.

——, D. B. Ross and C. L. Rufenach, 1981: On the detectability of

ocean surface waves by real and synthetic aperture radar. *J. Geophys. Res.*, 86, 6481–6498.

Anderson, D., A. Hollingworth, S. Uppala and P. Woiceshyn, 1987: A study of the feasibility of using sea and wind information from the ERS-1 satellite. *ESA Rep., Part I.*

Atlas, R., A. J. Busalachi, M. Ghil, S. Bloom and E. Kalnay, 1987: Global surface wind and flux fields from model assimilation of SEASAT data. *J. Geophys. Res.*, 92, 6477–6487.

Beal, R. C., T. W. Gerling, D. E. Irvine, F. M. Monaldo and D. G. Tilley, 1986: Spatial variations of ocean wave directional spectra from SEASAT synthetic aperture radar. *Geophys. Res.*, 91, 2433–2449.

Bertotti, L., A. Guillaume and P. Janssen, 1986: The WAMS Project—first test of a shallow water, third generation model against data. Unpublished rep. [Available from KNMI, P.O. Box 201, 3730 AE De Bilt, The Netherlands.]

Booij, N., and L. H. Holthuijsen, 1987: Propagation of ocean waves in discrete spectral models. *J. Comput. Phys.*, 68, 307–326.

Brüning, C., W. Alpers and K. Hasselmann, 1988: Monte Carlo simulation studies of the nonlinear imaging of a two-dimensional surface wave field by a synthetic aperture radar. Submitted to *Int. J. Rem. Sensing.*

Cardone, V. J., and D. B. Ross, 1979: State-of-the-art wave prediction methods and data requirements. *Ocean Wave Climate*, M. D. Earle and A. Malahoff, Eds., Plenum, 61–91.

——, W. J. Pierson and E. G. Ward, 1976: Hindcasting the directional spectrum of hurricane generated waves. *J. Petrol. Technol.*, 28, 385–394.

——, D. B. Ross and M. Ahrens, 1978: An experiment in forecasting hurricane generated sea states. *Proc. 11th Technical Conference on Hurricanes and Tropical Meteorology*, Miami Beach, Amer. Meteor. Soc.

——, C. V. Greenwood and J. A. Greenwood, 1979: A unified program for the specification of hurricane boundary layer winds over surfaces of specific roughness. Final Rep., Contract DACW-39-78-C-0100, Dept. of the Army, Waterways Experiment Station, Corps of Engineers, Vicksburg, MS.

Charnock, H., 1955: Wind stress on a water surface. *Quart. J. Roy. Meteor. Soc.*, 81, 639–640.

Donelan, M., 1987: The effect of swell on the growth of wind-waves. *Symp. on Measuring Ocean Waves from Space*, Baltimore, Johns Hopkins University.

——, and W. J. Pierson, 1983: The sampling variability of estimates of spectra of wind-generated gravity waves. *J. Geophys. Res.*, 88(C7), 4381–4392.

——, and ——, 1987: Radar scattering and equilibrium ranges in wind-generated waves—with application to scatterometry. *J. Geophys. Res.*, in press.

Forristall, G. Z., and A. M. Reece, 1985: Measurements of wave attenuation due to a soft bottom: The SWAMP Experiment. *J. Geophys. Res.*, 90(C2), 3367–3380.

——, R. C. Hamilton and V. J. Cardone, 1977: Continental shelf currents in tropical storm Delia: Observations and theory. *J. Phys. Oceanogr.*, 7, 532–546.

——, E. G. Ward, V. J. Cardone and L. E. Borgman, 1978: The directional spectra and kinematics of surface waves in Tropical Storm Delia. *J. Phys. Oceanogr.*, 8, 888–909.

——, —— and V. J. Cardone, 1980: Directional wave spectra and wave kinematics in hurricanes Carmen and Eloise. *17th Int. Conf. on Coastal Engineering*, Sydney, Australia.

Francis, P. E., J. J. Ephraums, C. H. Bracher and J. P. Thomas, 1985: Wave Hindcast Study (WHIST). Final Rep. by the Meteorological Office (Bracknell).

Gao, Q., 1986: Scientific Report KNMI.

Gelci, R., H. Cazalé and J. Vassal, 1957: Prévision de la houle. La méthode des densités spectroangulaires. *Bull. Infor. Comité Central Oceanogr. d'Etude Côtes*, 9, 416–435.

Groves, G. W., and J. Melcer, 1961: On the propagation of ocean waves on a sphere. *Geof. Int.*, 8, 77–93.

Hasselmann, D. E., M. Dunckel and J. A. Ewing, 1980: Directional

wave spectra observed during JONSWAP 1973. *J. Phys. Oceanogr.*, **10**, 1264–1280.

——, J. Bösenberg, M. Dunckel, K. Richter, M. Grünewald and H. Carlson, 1986: Measurements of wave-induced pressure over surface gravity waves. *Proc. IUCRM Symp. on Wave Dynamics and Radio Probing of the Ocean Surface*, Miami, O. M. Phillips and Klaus Hasselmann, eds., Plenum Press, 353–368.

Hasselmann, K., 1960: Grundgleichungen der Seegangsvoraussage. *Schiffstechnik*, **7**, 191–195.

——, 1974: On the spectral dissipation of ocean waves due to white capping. *Bound.-Layer Meteor.*, **6**, 107–127.

——, T. P. Barnett, E. Bouws, H. Carlson, D. E. Cartwright, K. Enke, J. A. Ewing, H. Gienapp, D. E. Hasselmann, P. Kruseman, A. Meerburg, P. Müller, D. J. Olbers, K. Richter, W. Sell and H. Walden, 1973: Measurements of wind-wave growth and swell decay during the Joint North Sea Wave Project (JONSWAP). *Dtsch. Hydrogr. Z.*, A **8**(12).

——, D. B. Ross, P. Müller and W. Sell, 1976: A parametric wave prediction model. *J. Phys. Oceanogr.*, **6**, 200–228.

——, S. Hasselmann, E. Bauer, C. Brüning, S. Lehner, H. Graber and P. Lionello, 1988: Satellite SAR image spectra and altimeter wave height data assimilation system for ERS-1. Final Rep., ESA Study Contract N°6875/87/HGE-I(SC).

Hasselmann, S., 1987: The WAM Wave Model System. Rep. Max-Planck-Institut für Meteorologie, Hamburg.

——, and K. Hasselmann, 1981: A symmetrical method of computing the nonlinear transfer in a gravity-wave spectrum. *Hamb. Geophys. Einzelschriften, Reihe A: Wiss. Abhand.*, **52**, 138 pp.

——, and ——, 1985: Computations and parameterizations of the nonlinear energy transfer in a gravity wave spectrum. Part I: A new method for efficient computations of the exact nonlinear transfer integral. *J. Phys. Oceanogr.*, **15**, 1369–1377.

——, ——, J. H. Allender and T. P. Barnett, 1985: Computations and parameterizations of the nonlinear energy transfer in a gravity-wave spectrum. Part II: Parameterizations of the nonlinear energy transfer for application in wave models. *J. Phys. Oceanogr.*, **15**, 1378–1391.

Janssen, P. A. E. M., and G. J. Komen, 1985: Effect of atmospheric stability on the growth of surface waves. *Bound.-Layer Meteor.*, **32**, 85–96.

——, —— and W. J. P. de Voogt, 1987: Friction velocity scaling in wind wave generation. *Bound.-Layer Meteor.*, **38**, 29–37.

——, P. Lionello, M. Reistad and A. Hollingsworth, 1987: Use of scatterometer wind and altimeter data. *Wave Modelling and Assimilation*. ESA Rep., Part II.

Kitaigorodskii, S. A., 1983: On the theory of the equilibrium range in the spectrum of wind-generated gravity waves. *J. Phys. Oceanogr.*, **13**, 816–827.

Komen, G. J., 1985: Activities of the WAM (Wave Modelling) Group. *Advances in Underwater Technology. Ocean Science and Offshore Engineering*, Vol. 6 *Oceanology*, 121–127, Graham and Trotman.

——, S. Hasselmann and K. Hasselmann, 1984: On the existence of a fully developed windsea spectrum. *J. Phys. Oceanogr.*, **14**, 1271–1285.

Lehner, S., 1984: The use of SAR for large scale wind measurements over the ocean. *Hamburger Geophys. Einzelschr.*, **74**.

——, and M. Lehner, 1988: SEASAT SAR ocean wave analysis for the northeast Atlantic. (in preparation).

Miles, J. W., 1957: On the generation of surface waves by shear flows. *J. Fluid Mech.*, **3**, 185–204.

Mitsuyasu, H., 1968: On the growth of the spectrum of wind-generated waves. 1. *Rep. Res. Inst. Appl. Mech., Kyushu University*, **16**, 459–465.

——, 1969: On the growth of the spectrum of wind-generated waves. 2. *Rep. Res. Inst. Appl. Mech., Kyushu University*, **17**, 235–243.

Mognard, N. M., W. J. Campbell, R. E. Cheney and J. G. Marsh, 1983: Southern ocean mean monthly waves and surface winds for winter 1978 by SEASAT radar altimeter. *J. Geophys. Res.*, **88**, 1736–1744.

Phillips, O. M., 1957: On the generation of waves by turbulent wind. *J. Fluid Mech.*, **2**, 417–445.

——, 1958: The equilibrium range in the spectrum of wind-generated ocean waves. *J. Fluid Mech.*, **4**, 426–434.

——, 1977: *Dynamics of the Upper Ocean*, 2nd ed., Cambridge University Press.

Raney, R. K., 1981: Wave orbital velocity, fade and SAR response to azimuth waves. *IEEE J. Oceanic Eng.*, OE-6, **4**.

Reece, A. M., and V. J. Cardone, 1982: Test of wave hindcast model results against measurements during four different meteorological systems. OTC (Offshore Technology Conference) 4323, 14th Annual OTC, Houston.

Ross, D. B., and V. J. Cardone, 1978: A comparison of parametric and spectral hurricane wave prediction products. *Turbulent Fluxes through the Sea Surface, Wave Dynamics, and Prediction*. A. Favre and K. Hasselmann, Eds., 647–665.

Shemdin, O., K. Hasselmann, S. V. Hsiao and K. Herterich, 1978: Nonlinear and linear bottom interaction effects in shallow water. *Proc. NATO Symp. on Turbulent Fluxes through the Sea Surface, Wave Dynamics, and Prediction*. Ile de Bendor, France, A. Favre and K. Hasselmann, Eds., Plenum Press.

Snyder, R. L., F. W. Dobson, J. A. Elliott and R. B. Long, 1981: Array measurements of atmospheric pressure fluctuations above surface gravity waves. *J. Fluid Mech.*, **102**, 1–59.

Steele, K. E., P. A. Wolfgram, A. Trampus and B. S. Graham, 1976: An operational high resolution wave data analyzer system for buoys. *Proc. Second Annual Combined Conf. Oceans '76*, Washington, DC, Marine Tech. Soc. and the IEEE.

The SWAMP Group, 1985: Sea Wave Modelling Project (SWAMP). An intercomparison study of wind wave prediction models, Part 1: Principal results and conclusions. *Ocean Wave Modeling*, Plenum Press, 256 pp.

Swift, C. F., and L. R. Wilson, 1979: Synthetic aperture radar imaging of moving ocean waves. *IEEE Trans. Antenn. Propag.*, AP 27, 725–729.

The SWIM Group: Bouws, E., J. J. Ephraums, J. A. Ewing, P. E. Francis, H. Günther, P. A. E. M. Janssen, G. J. Komen, W. Rosenthal and W. J. P. de Voogt, 1985: A shallow water intercomparison of three numerical wave prediction models (SWIM). *Quart. J. Roy. Meteor. Soc.*, **111**, 1087–1112.

Valenzuela, G. R., 1980: An asymptotic formulation for SAR images of the dynamical ocean surface. *Radio Sci.*, **15**, 105–114.

Ward, E. G., 1974: Ocean data gathering program—an overview OTC #2108-B, presented at the *Sixth Annual OTC*, Houston.

Weber, S. L., 1987: The energy balance of finite depth gravity waves. *J. Geophys. Res.*, **93**, 3601–3607.

Woiceshyn, P. M., M. G. Wurtele, D. H. Boggs, L. F. McGoldrick and S. Peteherych, 1987: The necessity for a new parameterization of an empirical model for wind/ocean scatterometry. *J. Geophys. Res.*, **91**, 2273–2288.

Young, I. R., S. Hasselmann and K. Hasselmann, 1987: Computations of the response of a wave spectrum to a sudden change in the wind direction. *J. Phys. Oceanogr.*, **17**, 1317–1338.

Zakharov, V. Y., and M. M. Zaslavskiy, 1982: The kinetic equation and Kolmogorov spectra in the weak turbulence theory of wind waves. *Izv. Atmos. Oceanic Phys.*, **18**, 747–753.